

Scaling regimes in spherical shell rotating convection

Thomas Gastine^{1,2†}, Johannes Wicht², Julien Aubert¹

¹Institut de Physique du Globe de Paris, Sorbonne Paris Cité, Université Paris-Diderot, UMR 7154 CNRS, 1 rue Jussieu, F-75005 Paris, France,

²Max Planck Institut für Sonnensystemforschung, Justus-von-Liebig-Weg 3, 37077 Göttingen, Germany.

(Received ?; revised ?; accepted ?. - To be entered by editorial office)

Rayleigh-Bénard convection in rotating spherical shells can be considered as a simplified analogue of many astrophysical and geophysical fluid flows. Here, we use three-dimensional direct numerical simulations to study this physical process. We construct a dataset of more than 200 numerical models that cover a broad parameter range with Ekman numbers spanning $3 \times 10^{-7} \leq E \leq 10^{-1}$, Rayleigh numbers within the range $10^3 < Ra < 2 \times 10^{10}$ and a Prandtl number unity. The radius ratio r_i/r_o is 0.6 in all cases and the gravity is assumed to be proportional to $1/r^2$. We investigate the scaling behaviours of both local (length scales, boundary layers) and global (Nusselt and Reynolds numbers) properties across various physical regimes from onset of rotating convection to weakly-rotating convection. Close to critical, the convective flow is dominated by a triple force balance between viscosity, Coriolis force and buoyancy. For larger supercriticalities, a small subset of our numerical data approaches the asymptotic diffusivity-free scaling of rotating convection $Nu \sim Ra^{3/2}E^2$ in a narrow fraction of the parameter space delimited by $6 Ra_c \leq Ra \leq 0.4 E^{-8/5}$. Using a decomposition of the viscous dissipation rate into bulk and boundary layer contributions, we establish a theoretical scaling of the flow velocity that accurately describes the numerical data. In rapidly-rotating turbulent convection, the fluid bulk is controlled by a triple force balance between Coriolis, inertia and buoyancy, while the remaining fraction of the dissipation can be attributed to the viscous friction in the Ekman layers. Beyond $Ra \simeq E^{-8/5}$, the rotational constraint on the convective flow is gradually lost and the flow properties continuously vary to match the regime changes between rotation-dominated and non-rotating convection. We show that the quantity $RaE^{12/7}$ provides an accurate transition parameter to separate rotating and non-rotating convection.

Key words: Bénard convection, geostrophic turbulence, rotating flows

1. Introduction

Convection-driven flows under the influence of rotation are an ubiquitous physical phenomenon in the fluid interiors of natural objects. The liquid iron core of terrestrial planets, the envelopes of gas giants, or the convective regions of rapidly-rotating cool stars harbour highly turbulent convective flows strongly constrained by the dominant role of the Coriolis force. Rayleigh-Bénard convection (hereafter RBC) is a classical framework

† Email address for correspondence: gastine@ipgp.fr

to examine the influence of rotation on turbulent convection. In its canonical form, rotating RBC consists of a planar fluid layer confined between two horizontal rigid plates separated from a distance L , rotating about the vertical axis with a constant rotation rate Ω . In this setup configuration, convective motions are driven by a fixed imposed temperature contrast ΔT between the two plates. The dynamics is then controlled by three dimensionless numbers, namely the Rayleigh number $Ra = \alpha_T g L^3 \Delta T / \nu \kappa$, the Ekman number $E = \nu / \Omega L^2$, and the Prandtl number $Pr = \nu / \kappa$, where ν and κ are the viscous and thermal diffusivities, α_T is the thermal expansivity and g is the gravity. A combination of these parameters, named the convective Rossby number $Ro_c = Ra^{1/2} E / Pr^{1/2}$, is frequently employed as a reasonable proxy of the ratio between the global-scale buoyancy and Coriolis forces (Gilman 1977). The key issue in RBC is to explore the efficiency of the heat and momentum transports across the layer. Important quantities in this regard are the Reynolds number Re and the dimensionless heat transport, defined by the Nusselt number $Nu = QL / \rho c_p \kappa \Delta T$, where Q is the total heat flux, ρ is the density and c_p the heat capacity. The Nusselt number is the most widely studied diagnostic since it can be easily measured experimentally and numerically and then compared to numerical and theoretical predictions. The understanding of the scaling dependence of Nu upon the control parameters Ra , E and Pr is of paramount importance to identify the different regimes and to possibly extrapolate the scaling behaviours to natural objects.

Rotational constraints delay the onset of convection and the critical Rayleigh number increases with increasing rotation rates as $Ra_c \sim E^{-4/3}$ when $E \rightarrow 0$ (Chandrasekhar 1961). The convective pattern takes the form of elongated Taylor columns which have a typical horizontal size $\ell \sim E^{1/3} L$ and are aligned with the rotation axis. Beyond Ra_c , the heat transport rises much more rapidly than for non-rotating convection (e.g. Rossby 1969; Boubnov & Golitsyn 1990). Hence, if the Rayleigh number is continuously increased far beyond Ra_c at a given Ekman number, the heat transfer properties will eventually transition to a state where rotational effects become secondary. In this weakly-rotating regime with $Ro_c \gg 1$, the scaling properties become essentially reminiscent to non-rotating RBC (e.g. Liu & Ecke 1997; Zhong *et al.* 2009). The heat transport scaling is then expected to become independent of the Ekman number and to approach the scalings obtained in classical RBC, i.e. $Nu \sim Ra^{\nu_{\text{eff}}}$, with $0.27 \leq \nu_{\text{eff}} \leq 1/3$ for $10^5 \leq Ra \leq 10^{12}$ (e.g. Grossmann & Lohse 2000; Funfschilling *et al.* 2005; Ahlers *et al.* 2009; Chillà & Schumacher 2012).

A turbulent regime of rotating convection is expected when both $Ro_c \ll 1$ and $Re \gg 1$. This implies large supercriticalities in combination with low Ekman numbers to ensure that the rotational constraints are not lost. This parameter range is therefore particularly difficult to explore with current-day laboratory experiments and numerical simulations (see Aurnou *et al.* 2015). In the following, we make the assumption that the heat transport scaling can be written as

$$Nu \sim Ra^\alpha E^\beta Pr^\gamma$$

in this regime. In general though, the values of the exponents α , β and γ might well continuously vary with Ra similarly to classical RBC (Grossmann & Lohse 2000). In contrast to non-rotating convection where the heat transport is controlled by diffusive processes in the thermal boundary layers, a dominant fraction of the temperature difference is accommodated in the fluid bulk when $Ro_c \ll 1$ (e.g. Boubnov & Golitsyn 1990; Schmitz & Tilgner 2009; Kunnen *et al.* 2010; Julien *et al.* 2012b; King *et al.* 2013). We can therefore hypothesise that the heat transport is controlled by the fluid bulk rather than by the thermal boundary layers that play an important role in the weakly-rotating limit. Because the viscous dissipation is rather weak in the fluid interior, we make the

assumption that Nu will thus become independent of the diffusivities ν and κ in the asymptotic limit of rapidly-rotating convection (Gillet & Jones 2006; Jones 2015). From the definition of Ra , E , Pr and Nu , this requirement yields the following combination of the scaling exponents

$$-\alpha + \beta + \gamma = 0, \quad \alpha + \gamma = 1.$$

In the limit of non-rotating convection, the dependence on E vanishes (i.e. $\beta = 0$) and the previous relationship between the scaling exponents relating α and γ yields the so-called *ultimate regime* of classical RBC $Nu \sim Ra^{1/2} Pr^{1/2}$ (Kraichnan 1962). Numerical models of rotating convection by King *et al.* (2012) further indicate that the heat flux might only depend on the supercriticality Ra/Ra_c when $Ro_c \ll 1$ (see also Julien *et al.* 2012a; Stellmach *et al.* 2014). This second hypothesis yields $\beta = 4\alpha/3$ when $E \rightarrow 0$ and allows us to derive the following diffusivity-free scaling for rotating convection

$$Nu \sim Ra^{3/2} E^2 Pr^{-1/2}. \quad (1.1)$$

Gillet & Jones (2006) derive the same equation under the hypothesis that a triple force balance between Coriolis force, inertia and buoyancy controls the asymptotic regime of rapidly-rotating turbulent convection (see also Stevenson 1979; Barker *et al.* 2014). The analysis carried out by Julien *et al.* (2012a) leads to the same inviscid scaling in the framework of asymptotically-reduced equations expected to hold when $E \rightarrow 0$. The evidence for such a low- Ro_c scaling law is however strongly debated. Specifically, King *et al.* (2012) suggest a much steeper heat transport scaling $Nu \sim Ra^3 E^4$ for $E = \mathcal{O}(10^{-5})$ and $Ro_c = \mathcal{O}(0.1)$, based on laboratory experiments in water complemented by numerical simulations of rotating convection with rigid mechanical boundaries in cartesian coordinates (see also King *et al.* 2013). Similar numerical models by Schmitz & Tilgner (2009) that instead employ stress-free boundaries rather found $Nu \sim (Ra E^{4/3})^{1.22}$ for a comparable parameter range. This discrepancy implies that the viscous boundary layers might still have a direct influence on the heat transport even at low E . The recent comparative study by Stellmach *et al.* (2014) for rigid and stress-free numerical models at lower Ekman numbers $E = \mathcal{O}(10^{-7})$ indeed reveals an active role of the Ekman boundary layers (see also Kunnen *et al.* 2016; Plumley *et al.* 2016). While the stress-free models gradually approach the diffusivity-free scaling (1.1) (see also Barker *et al.* 2014), the Ekman pumping in the cases with rigid boundaries leads to increasing scaling exponents when E is decreased towards geophysical values (Cheng *et al.* 2015; Julien *et al.* 2016). This prominent role of the boundary layers therefore questions the relevance of the inviscid scaling (1.1) for rigid boundaries.

Although the spherical geometry is more natural for studying rotating convection in astrophysical and geophysical objects, the majority of the rotating RBC laboratory experiments developed over the past three decades have been carried out in planar and cylindrical cells, in which the rotation axis and the gravity are aligned. The cartesian geometry also allows the computation of efficient local direct numerical simulations that operate at low Ekman numbers (e.g. Kunnen *et al.* 2010; Ecke & Niemela 2014; Horn & Shishkina 2015). Hence, the fruitful interplay between numerical and laboratory experiments in planar or cylindrical geometry enabled a complementary coverage of the parameter space in the low- Ro_c regime (e.g. Aurnou 2007; Stellmach *et al.* 2014; Cheng *et al.* 2015; Aurnou *et al.* 2015). However, it remains unclear whether the planar RBC results can be directly applied to rotating convection in spherical geometry. Two specific features of thermal convection in rotating spherical shells are indeed expected to yield significant dynamical differences with the planar or cylindrical RBC setups: (i) in most of the fluid volume of spherical shells, gravity is inclined with respect to the rotation

axis; (ii) due to both curvature and radial variations of the gravitational acceleration, spherical RBC features a significant asymmetry between the hot and the cold bounding surfaces (e.g. Bercovici *et al.* 1989; Jarvis 1993; Gastine *et al.* 2015).

Besides the micro-gravity experiments that operate at relatively large Ekman numbers due to their moderate sizes ($E = \mathcal{O}(10^{-3})$, see Hart *et al.* 1986; Egbers *et al.* 2003), most of the laboratory investigations of spherical rotating RBC make use of the centrifugal force as a surrogate for the radial gravitational acceleration (Busse & Carrigan 1974; Cardin & Olson 1994; Sumita & Olson 2003; Shew & Lathrop 2005). The combined influence of the laboratory gravity and the centrifugal acceleration of the rotating vessel indeed allows to generate surfaces of gravity potential close to the spherical surfaces in the lower hemisphere of the spherical shell (see for a review Cardin & Olson 2015). This technique was first employed to explore the onset of convection in rotating spherical RBC (Cordero & Busse 1992). Sumita & Olson (2003) studied the scaling behaviours of the heat transport for a relatively low Ekman number ($E \simeq 5 \times 10^{-6}$) but with a strong convective forcing ($Ra \geq 200 Ra_c$). In this parameter range, they obtained $Nu \sim Ra^{0.41}$, a scaling exponent that is hardly steeper than non-rotating RBC and therefore suggests that Coriolis force only plays a minor role on the heat transfer.

Numerical simulations of three-dimensional convection in spherical shells have been developed since the late 1970s as a complementary approach to the laboratory experiments (e.g. Gilman 1977; Tilgner & Busse 1997; Christensen 2002). Christensen & Aubert (2006), later complemented by King *et al.* (2010), conducted a systematic parameter study of the scaling properties of convective dynamo models with rigid boundaries and reported the scaling $Nu \sim Ra^{6/5} E^{8/5}$ for $E = \mathcal{O}(10^{-5})$. These studies were however carried out in the presence of a self-sustained magnetic field that can possibly impinge on the heat transport. More recently, Yadav *et al.* (2016) studied the influence of both the presence of a magnetic field and the nature of the mechanical boundary condition on the heat transfer in spherical RBC. Magnetic and non-magnetic models were found to exhibit similar heat transfer scaling behaviours possibly because of the parameter space limitation to $E = \mathcal{O}(10^{-5})$ (see also Soderlund *et al.* 2012; Garcia *et al.* 2014). Furthermore, these authors did not observe the steep increase of the Ra -scaling exponent beyond $3/2$ reported in the cartesian calculations (e.g. King *et al.* 2012) when rigid boundaries were employed. Since the heat transport in spherical shells is dominated by the equatorial regions where the gravity is nearly perpendicular to the rotation axis (Tilgner & Busse 1997; Yadav *et al.* 2016), it is not entirely surprising that the scaling properties differ from the cartesian models that would best represent the high-latitude dynamics of a spherical shell.

While Nu is an ubiquitous diagnostic quantity studied in both laboratory experiments and numerical models; numerical calculations also enable the computation of additional diagnostics that can provide direct insights on the dynamical regimes. In that regard, the scaling analysis of the convective flow speed Re and the typical length scale ℓ can be used to disentangle the underlying force balance in rotating RBC (Aubert *et al.* 2001; King & Buffett 2013). Two theoretical scalings for Re and ℓ have been put forward. The first one, frequently called the inertial scaling of rotating convection, hypothesises a triple force balance between Coriolis, inertia and Archimedean forces (CIA scaling, see Stevenson 1979; Cardin & Olson 1994; Aubert *et al.* 2001; Barker *et al.* 2014), while the second rather relies on a triple balance between viscosity, Archimedean and Coriolis forces (VAC scaling, see King *et al.* 2013). These two concurrent theories however lead to scaling exponents for $Re(Ra, E, Pr)$ close to each other. Using the numerical dataset by Christensen & Aubert (2006), King & Buffett (2013) even demonstrated that the limited data can support both Re -scalings at the same statistical confidence level.

This study indicates a sizeable role played by viscosity in rotating RBC models with $E \geq 10^{-5}$. To decrease the numerical cost of direct three-dimensional calculations, the quasi-geostrophic approximation of spherical convection (hereafter QG, see Busse & Or 1986; Cardin & Olson 1994) has been developed. In the limit of $E \rightarrow 0$ and $Ro_c \ll 1$, convection is strongly constrained by rotation and can be approximated by a quasi two-dimensional flow, which allows to decrease the Ekman number to $E = \mathcal{O}(10^{-7})$ (Aubert *et al.* 2003; Gillet & Jones 2006; Guervilly 2010). However, the scaling analyses carried out by Gillet & Jones (2006) and Guervilly (2010) did not show any clear evidence of convergence towards the diffusivity-free scalings for both Nu and Re , even when $E \lesssim 10^{-6}$. Furthermore, the lack of a direct one-to-one comparison between the QG results and the fully three-dimensional computations makes the interpretation of these results difficult. Hence, the determination of an accurate scaling law for both Re and ℓ in rapidly-rotating spherical RBC forms one of the main goals of this work.

The aims of this study are twofold: (i) determine the boundaries of the different physical regimes of rapidly-rotating convection in spherical shells by means of three-dimensional numerical simulations; (ii) establish the scaling behaviours of both the local (length scale, boundary layers) and the global (Nu and Re) properties that hold within each of these different regimes. We conduct a systematic parameter study varying the Ekman number within the range $3 \times 10^{-7} \leq E \leq 10^{-1}$ and the Rayleigh number within the range $10^3 \lesssim Ra \lesssim 2 \times 10^{10}$ for a unity Prandtl number spherical shell of radius ratio $r_i/r_o = 0.6$. To do so, we construct a dataset of 227 rotating simulations that complements our previous non-rotating calculations (Gastine *et al.* 2015). Recent improvements of pseudo-spectral numerical codes (Schaeffer 2013) enabled us to decrease the Ekman number to values comparable to those used in present-day local cartesian calculations. Our dataset allows us to determine the regime boundaries for rotating convection and to check the validity of the diffusivity-free scaling (1.1) in the low- E regime. We examine the scaling behaviours of seven different diagnostics: Nu and Re , the viscous dissipation rate, the typical flow length scale, the interior temperature gradient and the viscous and the thermal boundary layer thicknesses.

In § 2, we introduce the hydrodynamical model and the various diagnostic quantities of interest. The numerical results are presented in § 3. We conclude with a summary of our findings in § 4.

2. Formulation of the hydrodynamical problem

2.1. Governing equations

We consider rotating convection of a Boussinesq fluid confined in a spherical shell that rotates at a constant frequency Ω about the z axis. Convective motions are driven by a fixed temperature contrast $\Delta T = T_i - T_o$ between the inner radius r_i and the outer radius r_o . The boundaries are impermeable, no slip and held at constant temperatures. We adopt a dimensionless formulation of the Navier-Stokes equations using the shell thickness $L = r_o - r_i$ as the reference length scale and the viscous diffusion time L^2/ν as the reference timescale. The temperature contrast ΔT defines the temperature scale and gravity is non-dimensionalised using its reference value at the outer boundary g_o . The dimensionless equations that govern convective motions for the velocity \mathbf{u} , the pressure p and the temperature T are then expressed by

$$\nabla \cdot \tilde{\mathbf{u}} = 0, \quad (2.1)$$

$$\frac{\partial \tilde{\mathbf{u}}}{\partial t} + \tilde{\mathbf{u}} \cdot \nabla \tilde{\mathbf{u}} + \frac{2}{E} \mathbf{e}_z \times \tilde{\mathbf{u}} = -\nabla \tilde{p} + \frac{Ra}{Pr} \tilde{g} \tilde{T} \mathbf{e}_r + \Delta \tilde{\mathbf{u}}, \quad (2.2)$$

$$\frac{\partial \tilde{T}}{\partial t} + \tilde{\mathbf{u}} \cdot \nabla \tilde{T} = \frac{1}{Pr} \Delta \tilde{T}, \quad (2.3)$$

where the tildes designate the dimensionless variables. The units vectors in the radial and vertical directions are denoted by \mathbf{e}_r and \mathbf{e}_z , respectively. We make the assumption of a centrally-condensed mass which yields a dimensionless gravity profile of the form $\tilde{g} = (r_o/r)^2$. This particular choice is motivated by the exact analytical relation between the buoyancy power and the so-called flux-based Rayleigh number when $\tilde{g} \sim 1/r^2$ (see below and Gastine *et al.* 2015). This enables us to conduct an exact analysis of the viscous dissipation rate and to directly compare our numerical models with our previous calculations of non-rotating convection which employed the same gravity profile.

The dimensionless equations (2.1-2.3) are governed by the Ekman number E , the Rayleigh number Ra , the Prandtl number Pr and the radius ratio of the spherical shell η defined by

$$E = \frac{\nu}{\Omega L^2}, \quad Ra = \frac{\alpha_T g_o \Delta T L^3}{\nu \kappa}, \quad Pr = \frac{\nu}{\kappa}, \quad \eta = \frac{r_i}{r_o}, \quad (2.4)$$

where α_T is the thermal expansion coefficient, ν is the kinematic viscosity and κ is the thermal diffusivity. In the following, we will also consider the convective Rossby number, Ro_c , expressed by

$$Ro_c = \sqrt{\frac{\alpha_T g_o \Delta T}{\Omega^2 L}} = \frac{Ra^{1/2} E}{Pr^{1/2}}, \quad (2.5)$$

which provides a good proxy of the relative importance of buoyancy forcing and Coriolis force in rotating convection (e.g. Gilman 1977).

2.2. Numerical technique

The numerical simulations carried out in this study have been computed using the open-source magnetohydrodynamics code MagIC[†] (Wicht 2002; Gastine *et al.* 2016). MagIC has been validated via several benchmark tests for convection and dynamo action in spherical shell geometry (Christensen *et al.* 2001; Jones *et al.* 2011). To solve the system of equations (2.1-2.3) in spherical coordinates (r, θ, ϕ) , the velocity field is decomposed into a poloidal and a toroidal contribution

$$\tilde{\mathbf{u}} = \nabla \times (\nabla \times \tilde{W} \mathbf{e}_r) + \nabla \times \tilde{Z} \mathbf{e}_r,$$

where \tilde{W} and \tilde{Z} are the poloidal and toroidal potentials. The dimensionless unknowns \tilde{W} , \tilde{Z} , \tilde{p} and \tilde{T} are expanded in spherical harmonic functions up to degree l_{\max} in the colatitude θ and longitude ϕ and in Chebyshev polynomials up to degree N_r in the radial direction. The equations are time-advanced using an explicit second-order Adams-Bashforth scheme for the Coriolis acceleration and the non-linear terms and an implicit Crank-Nicolson algorithm for the remaining linear terms. The explicit treatment of the Coriolis force implies that the dimensionless time-step size is limited to a fraction of the rotation period. For a comprehensive description of the numerical method and the associated spectral transforms, the reader is referred to Gilman & Glatzmaier (1981); Tilgner & Busse (1997) and Christensen & Wicht (2015). For the most demanding calculations, MagIC uses the open-source library SHTns[‡] to speed-up the spherical harmonic transforms (Schaeffer 2013).

[†] Available at <http://www.github.com/magic-sph/magic>

[‡] Available at <https://bitbucket.org/nschaeff/shtns>

2.3. Diagnostics

We introduce in the following several diagnostic properties to quantify the impact of the different control parameters on the flow and temperature properties. We adopt several notations regarding averaging procedures. Overbars $\overline{\cdots}$ correspond to temporal averaging, angular brackets $\langle \cdots \rangle$ to spatial averaging over the entire spherical shell volume and $\langle \cdots \rangle_s$ to an average over a spherical surface

$$\overline{f} = \frac{1}{\tau} \int_{t_0}^{t_0+\tau} f \, dt, \quad \langle f \rangle = \frac{1}{V} \int_V f(r, \theta, \phi) \, dV, \quad \langle f \rangle_s = \frac{1}{4\pi} \int_0^\pi \int_0^{2\pi} f(r, \theta, \phi) \sin \theta \, d\theta \, d\phi,$$

where V is the spherical shell volume and τ is the time averaging interval.

For the sake of clarity, we introduce the notation ϑ to define the time and horizontally-averaged radial dimensionless temperature profile

$$\vartheta(r) = \overline{\langle \tilde{T} \rangle_s}.$$

The heat transport is characterised by the Nusselt number Nu , the ratio of the total heat flux to the heat carried by conduction

$$Nu = \frac{\eta \mathcal{Q} L}{\rho c_p \kappa \Delta T} = \frac{\left. \frac{d\vartheta}{dr} \right|_{r=r_o}}{\left. \frac{d\tilde{T}_c}{dr} \right|_{r=r_o}} = \frac{\left. \frac{d\vartheta}{dr} \right|_{r=r_i}}{\left. \frac{d\tilde{T}_c}{dr} \right|_{r=r_i}}, \quad (2.6)$$

where \mathcal{Q} is the heat flux, c_p is the heat capacity and \tilde{T}_c is the dimensionless conductive temperature profile, solution of

$$\frac{d}{dr} \left(r^2 \frac{d\tilde{T}_c}{dr} \right) = 0, \quad \tilde{T}_c(r_i) = 1, \quad \tilde{T}_c(r_o) = 0. \quad (2.7)$$

The dimensionless kinetic energy \tilde{E}_k is defined by

$$\tilde{E}_k = \frac{1}{2} \overline{\langle \tilde{u}^2 \rangle} = \sum_{l=1}^{l_{\max}} \sum_{m=0}^l \mathcal{E}_l^m,$$

where \mathcal{E}_l^m is the dimensionless kinetic energy density at a spherical harmonic degree l and order m . In rotating spherical shells, the axisymmetric zonal flow can represent a significant fraction of the total kinetic energy (e.g. Christensen 2002; Gastine & Wicht 2012; Yadav *et al.* 2016). Since this flow does not directly contribute to the heat transfer, we decide to rather characterise the r.m.s. flow velocity by the time-averaged convective Reynolds number expressed by

$$Re_c = \sqrt{2 \sum_{l=1}^{l_{\max}} \sum_{m=1}^l \mathcal{E}_l^m}, \quad (2.8)$$

where the contribution from the axisymmetric flows ($m = 0$) has been excluded. The fluid bulk in rotating convection usually departs from the well-mixed convective interior obtained in classical RBC. Under the influence of rapid rotation, turbulent mixing is inhibited and strong interior temperature gradients can persist (e.g. Julien *et al.* 1996; King *et al.* 2009; Stellmach *et al.* 2014). We denote the bulk temperature gradient at

mid-shell by

$$\beta_T = \left. \frac{d\vartheta}{dr} \right|_{r=r_m}, \quad r_m = \frac{1+\eta}{2(1-\eta)}. \quad (2.9)$$

Following Christensen & Aubert (2006), the typical flow length scale is determined from the time-averaged kinetic energy spectrum

$$\ell^{-1} = \left(\frac{L \sum_{l=1}^{l_{\max}} \sum_{m=0}^l l \mathcal{E}_l^m(t)}{\pi \sum_{l=1}^{l_{\max}} \sum_{m=0}^l \mathcal{E}_l^m(t)} \right). \quad (2.10)$$

Several different approaches have been usually considered to define the thermal boundary layer thickness λ_T . They either rely on the mean radial temperature profile $\vartheta(r)$ (e.g. Verzicco & Camussi 1999; Breuer *et al.* 2004; Liu & Ecke 2011) or on the root mean square of the temperature fluctuations (e.g. Julien *et al.* 2012b; King *et al.* 2013; Kunnen *et al.* 2016). For consistency with the definition adopted in our non-rotating calculations (Gastine *et al.* 2015), λ_T^i (λ_T^o) is defined here as the depth where the linear fit to the temperature profile near the inner (outer) boundary intersects the linear fit to the profile at mid-depth. The comparison of this boundary layer definition with the estimate coming from the location of the peaks of the r.m.s. of the temperature fluctuations for a few selected cases yield similar boundary layer thicknesses. The viscous boundary layer thicknesses are estimated following a similar slope-intersection method: λ_U^i (λ_U^o) is defined as the distance from the inner (outer) boundary where the linear fit to the horizontal velocity profile $u_h = \sqrt{u_\theta^2 + u_\phi^2}$ near the inner (outer) boundary intersects the horizontal line passing through the maximum of u_h (see also Breuer *et al.* 2004).

2.4. Parameter choice and resolution checks

We aim at studying the scaling behaviours of both the local (length scales, temperature gradient, boundary layers) and the global (Nusselt and Reynolds numbers) properties for each dynamical regimes of rotating convection in spherical shells. To achieve this goal, we build a dataset of 227 global spherical shell models that span the range $3 \times 10^{-7} \leq E \leq 10^{-1}$ and $10^3 < Ra < 2 \times 10^{10}$. The radius ratio η is kept fixed to $\eta = 0.6$ and the Prandtl number to $Pr = 1$ to limit the extension of the parameter space. This setup also allows a direct comparison with our previous non-rotating models (Gastine *et al.* 2015). The numerical dataset constructed in this study thoroughly explores various dynamical regimes of rotating convection encompassing convection close to critical, turbulent quasi-geostrophic convection and weakly-rotating convection. The summary table A1 given in the appendix contains the calculations of the main control and diagnostic quantities computed for each numerical simulation.

Particular attention must be paid to the numerical resolution requirements for global models of convection (Shishkina *et al.* 2010; King *et al.* 2012), since under-resolution can significantly degrade the accuracy of the obtained exponents when deriving asymptotic scaling laws (Amati *et al.* 2005). The comparison of the viscous and thermal dissipation rates with the time-averaged Nusselt number provides a robust way to validate the numerical resolutions employed in our models (e.g. Stevens *et al.* 2010; Lakkaraju *et al.* 2012). As demonstrated in our previous RBC calculations (Gastine *et al.* 2015), the choice of a centrally-condensed mass (i.e. $\tilde{g} \sim 1/r^2$) ensures the following analytical relations between the dimensionless viscous dissipation rate $\tilde{\epsilon}_U$ and the flux-based Rayleigh

number defined by $Ra_Q = Ra(Nu - 1)$:

$$\tilde{\epsilon}_U = \overline{\langle (\nabla \times \tilde{\mathbf{u}})^2 \rangle} = \frac{3}{1 + \eta + \eta^2} \frac{Ra_Q}{Pr^2}, \quad (2.11)$$

and between the dimensionless thermal dissipation rate $\tilde{\epsilon}_T$ and the Nusselt number

$$\tilde{\epsilon}_T = \overline{\langle (\nabla \tilde{T})^2 \rangle} = \frac{3\eta}{1 + \eta + \eta^2} Nu. \quad (2.12)$$

The related ratios

$$\chi_T = \frac{(1 + \eta + \eta^2) \tilde{\epsilon}_T}{3\eta Nu}, \quad \chi_U = \frac{(1 + \eta + \eta^2) Pr^2 \tilde{\epsilon}_U}{3 Ra_Q},$$

can thus be used to check the adequacy of the spatial resolutions of the numerical models. As shown in table A1, these ratios are very close to unity (within 3%) for all the simulations computed here, validating the grid resolutions. The temporal convergence of the numerical models has been ensured by running the simulations at least 50 convective overturn time.

The numerical truncations employed here range from ($N_r = 61$, $l_{\max} = 64$) for the case with the largest Ekman and lowest Rayleigh numbers to ($N_r = 641$, $l_{\max} = 1345$) for the numerical model with $E = 3 \times 10^{-7}$ and the highest Ra . To save computational resources, some of the most demanding cases (with $E \leq 3 \times 10^{-6}$) have been computed on an azimuthally truncated spherical shell with a two-fold, four-fold or eight-fold symmetry (see table A1 for details). Since rapidly-rotating convection is dominated by small-scale structures, this assumption is not considered to have any significant impact on the results. In addition, the comparison of test cases with or without symmetries showed no statistical differences. The total computational time spent to construct the present dataset of numerical models corresponds to roughly 13 millions core hours of Intel Ivy Bridge CPUs.

3. Numerical results

Figure 1 shows Nu as a function of Ra for both rotating and non-rotating cases. In rotating convection, the onset is delayed and the critical Rayleigh number Ra_c increases with decreasing Ekman number. Close to critical, Nu initially increases slowly and roughly linearly with Ra (dashed line). Beyond this weakly non-linear regime of rotating convection, i.e. when $Nu \gtrsim 2$, the heat transport increases more rapidly with Ra than in the non-rotating RBC (dotted-dashed line). This behaviour is reminiscent to that observed in plane layer studies (e.g. Rossby 1969; King *et al.* 2009; Schmitz & Tilgner 2009; Cheng *et al.* 2015). Above a transitional Rayleigh number that will be determined below, the heat transfer data for each Ekman number then tends towards the non-rotating behaviour. As shown in our previous study (Gastine *et al.* 2015), the non-rotating data ($E = \infty$) can be accurately described by a dissipation analysis that follows the Grossmann & Lohse (2000) theory (black circles and solid black line). The non-rotating RBC thus defines an effective upper limit for the heat transport in rotating convection in spherical shells at large Ra . In contrast to plane layer calculations, the spherical shell data do not exhibit any overshoot of rotating heat transfer beyond the non-rotating RBC scalings (Liu & Ecke 1997; Zhong *et al.* 2009).

To illustrate the diversity of the dynamical regimes in rotating spherical shell RBC, figure 2 shows equatorial, meridional and radial cuts of the dimensionless temperature fluctuation $\tilde{T}' = \tilde{T} - \vartheta$ for four selected cases. The filled-in symbols in figure 1 indicate

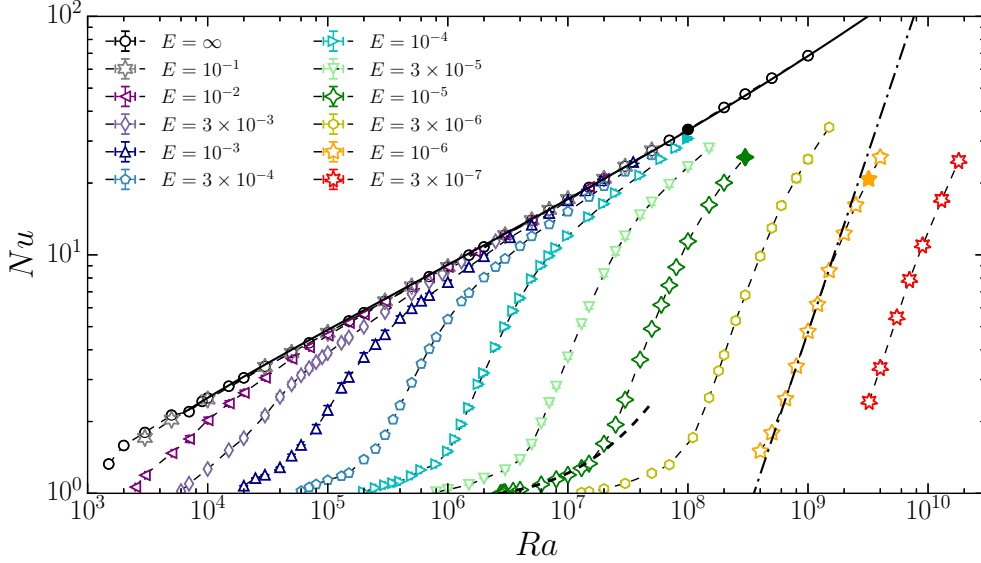


FIGURE 1. Nusselt number as a function of the Rayleigh number with Ekman numbers denoted by symbol shape (and colour online). The dashed black line corresponds to the weakly non-linear onset scaling $Nu - 1 = 0.08 (Ra/Ra_c - 1)$ (Equation 3.2) discussed in § 3.1. The dot-dashed black line to the asymptotic scaling $Nu = 0.15 Ra^{3/2} E^2$ (Equation 3.8) in the rotation-dominated regime discussed in § 3.2. The solid black line corresponds to heat transfer scaling for non-rotating convection derived in Gastine *et al.* (2015). The four filled-in symbols correspond to the four cases highlighted in figure 2. The error bars correspond to one standard-deviation from the time-averaged Nusselt number (i.e. $Nu \pm \sigma$). For most of the numerical models, these error bars are smaller than the size of the symbols.

their positions in the $Nu - Ra$ parameter space. The image in panel (a) corresponds to a non-rotating model with $Ra = 10^8$. Due to an efficient turbulent mixing, the fluid-bulk is nearly isothermalised and most of the temperature fluctuations take the form of thermal plumes that depart from the thin boundary layers. As visible on both spherical surfaces, the plume network is organised in long and thin sheet-like structures. Panel (b) corresponds to a numerical simulation with $E = 10^{-4}$ and $Ra = 10^8$, i.e. $Ro_c = 1$. The turbulent flow remains essentially anisotropic and three-dimensional with a typical length scale comparable to that in the non-rotating model. At the connection points of the convective lanes network, we nevertheless observe the formation of vortical structures, which indicates the influence of the Coriolis force on the largest scale. Panel (c) shows a numerical model with $E = 10^{-5}$ and $Ra = 3 \times 10^8$. In the equatorial region, columnar structures aligned with the rotation axis are observed. At high-latitudes, the integrity of the convective features is disrupted. This gradual loss of geostrophy is expected when the buoyancy forcing increases in strength with respect to the rotational constraint (here $Ro_c = 0.17$). The image in panel (d) corresponds to a numerical model with $E = 10^{-6}$ and $Ro_c = 0.05$. As compared to the previous model, the stronger rotational influence on the flow results in a more pronounced alignment of the convective features with the rotation axis. Decreasing the Ekman number from 10^{-5} (panel c) to 10^{-6} (panel d) is accompanied by an obvious decrease of the typical convective flow length scale. In the rapidly-rotating regime when $Ro_c \ll 1$, Coriolis forces inhibit the turbulent mixing and the fluid bulk therefore departs from an isothermal state.

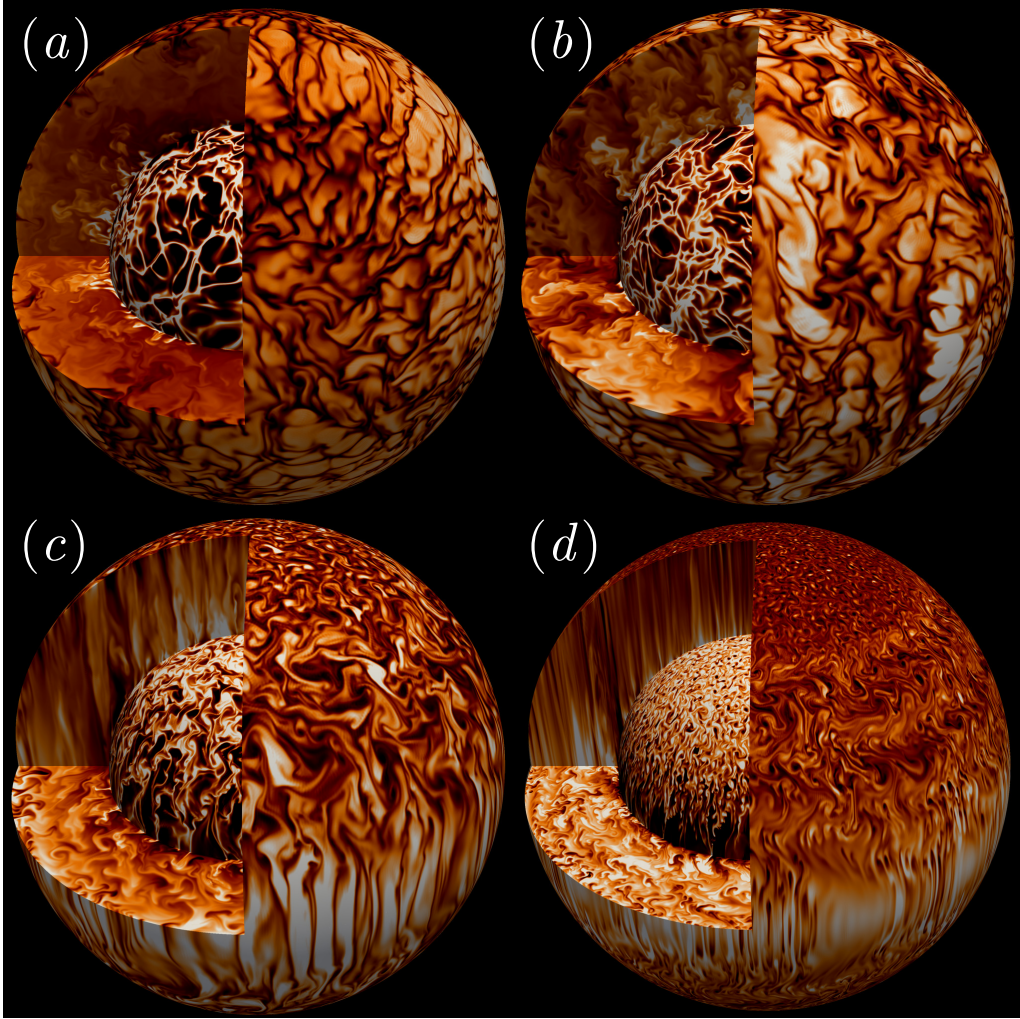


FIGURE 2. Meridional sections, equatorial cut and radial surfaces of the temperature fluctuations $\tilde{T}' = \tilde{T} - \vartheta$. The inner (outer) surface corresponds to the location of the inner (outer) thermal boundary layer $r = r_i + \lambda_T^i$ ($r = r_o - \lambda_T^o$). Color levels range from -0.15 (black) to 0.15 (white). Panel (a) corresponds to a non-rotating model with $Ra = 10^8$ (Gastine *et al.* 2015). Panel (b) corresponds to a numerical model with $E = 10^{-4}$ and $Ro_c = 1$ (Case 146 in table A1). Panel (c) corresponds to a numerical model with $E = 10^{-5}$ and $Ro_c = 0.17$ (Case 191 in table A1). Panel (d) corresponds to a numerical model with $E = 10^{-6}$ and $Ro_c = 0.05$ (Case 219 in table A1).

3.1. Weakly non-linear regime of rotating convection

In rotating spherical shells, the convective flow at onset takes the form of prograde drifting thermal Rossby waves that first develop in the vicinity of the tangent cylinder (e.g. Busse 1970; Dormy *et al.* 2004). The critical Rayleigh number Ra_c and azimuthal wavenumber m_c follow

$$Ra_c \sim E^{-4/3}, \quad m_c \sim E^{-1/3}. \quad (3.1)$$

The exact values of Ra_c and m_c for the different Ekman numbers considered in this study are given in table B1. For marginally supercritical Rayleigh numbers, the weakly non-linear perturbation analysis carried out by Busse & Or (1986) and Gillet & Jones

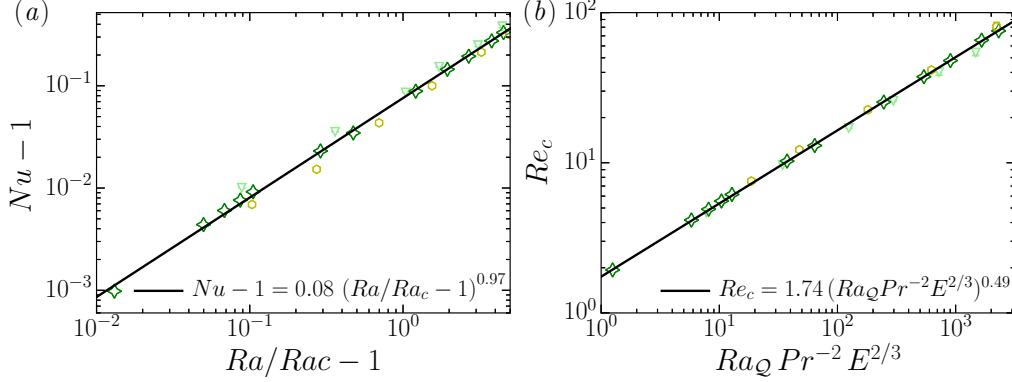


FIGURE 3. (a) Nusselt number $Nu - 1$ as a function of $Ra/Ra_c - 1$. (b) Reynolds number Re_c as a function of $Ra_Q Pr^{-2} E^{2/3}$. Only the cases with $E \leq 3 \times 10^{-5}$ and $Ra \leq 6 Ra_c$ are displayed in this figure. In both panels, the solid black lines correspond to the least-square fits to the data. The symbols have the same meaning as in figure 1.

(2006) predicted that the heat transport increases linearly with the supercriticality, i.e.:

$$Nu - 1 \sim \frac{Ra}{Ra_c} - 1. \quad (3.2)$$

Figure 3(a) shows $Nu - 1$ as a function of $Ra/Ra_c - 1$ for the numerical simulations with $E \leq 3 \times 10^{-5}$ and $Ra \leq 6 Ra_c$. The best-fit to the data yields $Nu - 1 = 0.076(\pm 0.003)(Ra/Ra_c - 1)^{0.973(\pm 0.019)}$. In spite of a remaining weak dependence on the Ekman number, the scaling (3.2) holds reasonably well for the numerical models with $Ra \leq 6 Ra_c$.

A useful tool for establishing a scaling for the typical convective flow speed (Re_c) is the linear relation between the viscous dissipation rate ϵ_U and the flux-based Rayleigh number Ra_Q given in (2.11). For a laminar flow close to the onset of convection, ϵ_U can be approximated by

$$\epsilon_U \sim \nu \frac{U_c^2}{\ell_\perp^2}, \quad (3.3)$$

where ℓ_\perp is the typical flow length scale and U_c the typical velocity. Close to the onset of convection, ℓ_\perp remains close to the critical azimuthal wavenumber, such that

$$\ell_\perp/L \sim 1/m_c \sim E^{1/3}. \quad (3.4)$$

Combining (2.11), (3.3) and (3.4) yields a scaling law for the convective flow speed $Re_c \sim U_c L/\nu$

$$Re_c \sim Ra_Q^{1/2} Pr^{-1} E^{1/3}. \quad (3.5)$$

This scaling relation is sometimes called the *Visco-Archimedean-Coriolis* (hereafter VAC) scaling and can also be directly derived from the balance between these three forces (Aubert *et al.* 2001; King & Buffett 2013; King *et al.* 2013). Figure 3(b) shows Re_c versus $Ra_Q Pr^{-2} E^{2/3}$ for the numerical simulations with $E \leq 3 \times 10^{-5}$ and $Ra \leq 6 Ra_c$. The least-square fit to the data yields $Re_c = 1.744(\pm 0.041)(Ra_Q E^{2/3})^{0.487(\pm 0.004)}$, in excellent agreement with the theoretical scaling.

Figure 4(a) shows the average flow length scale ℓ/L plotted as a function of E for the numerical models close to the onset of convection. The typical scale of convection gradually approaches the theoretical scaling $\ell/L \sim E^{1/3}$ when $E \leq 10^{-5}$ and the additional Ra dependence vanishes. The compensated scaling displayed in panel (b) suggests

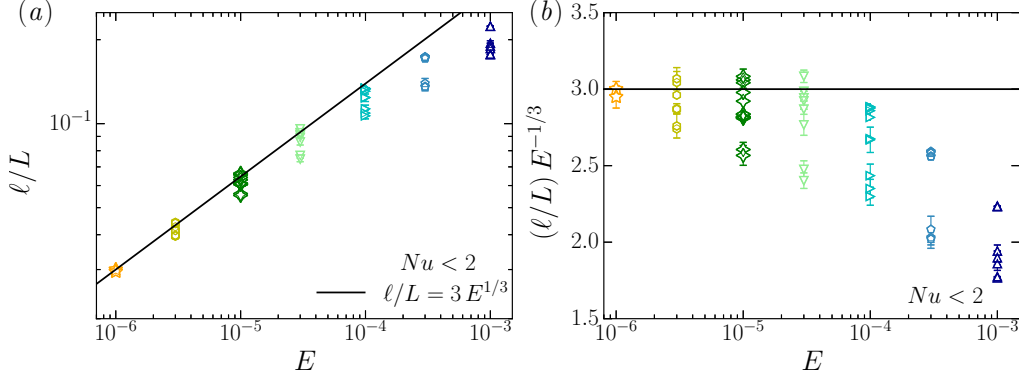


FIGURE 4. (a) Average flow length scale ℓ/L calculated using (2.10) as a function of the Ekman number for the numerical models close to the onset of convection with $Nu \leq 2$ and $E \leq 10^{-3}$. (b) Corresponding compensated ℓ/L scaling. In both panels, the solid black lines correspond to $\ell/L = 3E^{1/3}$ (Equation 3.4). The error bars illustrate the r.m.s. fluctuations and correspond to one standard-deviation from the time-averages. The symbols have the same meaning as in figure 1.

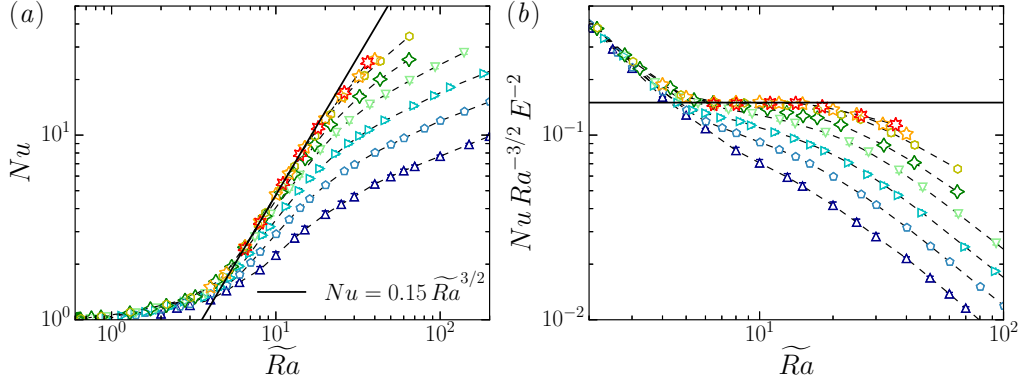


FIGURE 5. (a) Nusselt number as a function of $\widetilde{Ra} = RaE^{4/3}$. (b) Corresponding compensated Nu scaling. In both panels, the solid black line corresponds to the scaling $Nu = 0.15 \widetilde{Ra}^{3/2} E^2$ (Equation 3.8). For clarity, only the cases with $E \leq 10^{-3}$ and $\widetilde{Ra} < 200$ are displayed in this figure. The symbols have the same meaning as in figure 1.

the asymptotic scaling $\ell \simeq 3E^{1/3}L$. The cases with the largest Ekman number (i.e. $E \geq 10^{-4}$) significantly depart from this asymptotic law. This is not surprising since the scaling $m_c \sim E^{-1/3}$ is expected to hold for asymptotically-small Ekman numbers (see table B1).

3.2. Non-linear regime of rotating convection

3.2.1. Nusselt number scaling

As can be seen on figure 1, the weakly non-linear scaling (3.2) provides an accurate description of the heat transport behaviour up to $Nu \simeq 1.5$, which roughly corresponds to $Ra \simeq 6Ra_c$. When $Nu > 2$, the heat transport increases much more rapidly and enters the non-linear regime of rotating convection.

The plane layer numerical simulations of rotating convection by King *et al.* (2012) and Stellmach *et al.* (2014) as well as the asymptotically-reduced theoretical models by Julien *et al.* (2012a) indicate that the convective heat flux only depends on the

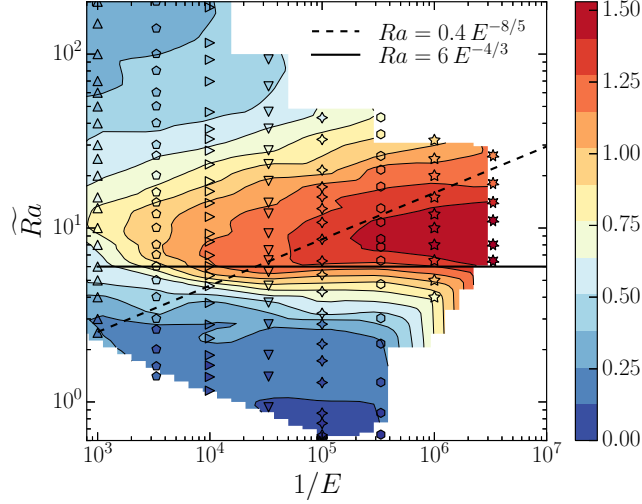


FIGURE 6. Isocontours of the local effective exponent α_{eff} of the $Nu = Ra^{\alpha_{\text{eff}}} E^{\beta_{\text{eff}}}$ scaling in the $(1/E, \widetilde{Ra})$ -plane. The symbol shape corresponds to the Ekman number as in the previous figures, while the symbol color scales here with the value of local slope α_{eff} . The solid black line corresponds to the upper limit of the weakly non-linear regime $Ra = 6 E^{-4/3}$, while the dashed black line corresponds to the dynamical boundary $Ra = 0.4 E^{-8/5}$ derived in figure 7.

supercriticality Ra/Ra_c when $Ro_c \ll 1$. To check whether our numerical calculations actually support such a behaviour at low Ekman numbers, figure 5(a) shows Nu as a function of $\widetilde{Ra} = Ra E^{4/3}$, since $Ra_c \sim E^{-4/3}$. For $\widetilde{Ra} < 6$, Nu slowly increases with the Rayleigh number and follows the previously described weakly non-linear regime. Beyond this point, a fast steepening of the slope is observed and the function $Nu = f(\widetilde{Ra})$ starts to show an additional dependence on E : while the large Ekman number cases quickly depart from a pure function of \widetilde{Ra} , the low Ekman number simulations continue to follow a law of the form $Nu = f(\widetilde{Ra})$ up to higher \widetilde{Ra} values. The exact location of this departure point gradually shifts to increasing \widetilde{Ra} with decreasing E . Figure 5(b) shows the compensated scalings of Nu and reveals that the steepest part of the heat transfer law approaches the diffusivity-free scaling $Nu = 0.15 \widetilde{Ra}^{3/2}$, at least in the range $6 \leq \widetilde{Ra} \leq 20$. To further assess the validity domain of the diffusivity-free scaling (1.1) in our numerical dataset, we introduce the local effective exponents α_{eff} and β_{eff} of the $Nu(Ra, E)$ law:

$$\alpha_{\text{eff}} = \left(\frac{\partial \ln Nu}{\partial \ln Ra} \right)_E; \quad \beta_{\text{eff}} = \left(\frac{\partial \ln Nu}{\partial \ln E} \right)_{Ra}. \quad (3.6)$$

The local exponent β_{eff} is unfortunately difficult to constrain since our dataset only samples sparse variations of the Ekman number (half-decade sampling). However, the dense coverage in Ra for each Ekman number subset allows to estimate the variations of α_{eff} . Figure 6 shows isocontours of α_{eff} in a $(1/E, \widetilde{Ra})$ -plane. Beyond the weakly non-linear regime delimited by the horizontal solid black line, the effective slope gradually increases with decreasing E . It reaches a maximum value $\alpha_{\text{eff}} \simeq 3/2$ for a small region around $E \lesssim 10^{-6}$ and $\widetilde{Ra} \simeq 10$.

The numerical simulations carried out by Cheng *et al.* (2015) in cartesian coordinates revealed a continuous increase of the local exponent α_{eff} with decreasing E and exhibit much steeper scaling beyond $\alpha_{\text{eff}} \simeq 3$ (see also Stellmach *et al.* 2014; Kunnen *et al.*

2016). This phenomenon has been attributed to the sizeable role of Ekman pumping that enhances the heat transfer even in the low Ekman number regime (Julien *et al.* 2016). This steep scaling is not observed in absence of Ekman boundary layers, for instance when stress-free mechanical boundary conditions are adopted (Stellmach *et al.* 2014; Barker *et al.* 2014; Kunnen *et al.* 2016; Plumley *et al.* 2016). In that case, local exponents close to $\alpha_{\text{eff}} \simeq 3/2$ are recovered at low Ekman numbers.

The scaling exponents obtained in our simulations in spherical geometry for comparable Ekman numbers $E = \mathcal{O}(10^{-7})$ remain bounded by the diffusivity-free scaling $\alpha_{\text{eff}} = 3/2$ (see also King *et al.* 2010). Although a further increase of α_{eff} for $E < 3 \times 10^{-7}$ cannot be *a priori* ruled out, the compensated scaling shown in figure 5(b) suggests a gradual approach to $\alpha = 3/2$, which seems to leave little room for further increase. This suggests that our simulations approach the asymptotic diffusivity-free behaviour for the parameter range $E \leq 10^{-6}$ and $6 \leq \widetilde{Ra} \leq 20$.

Clearly, though, the validity domain of the diffusivity-free scaling (1.1) remains relatively narrow in our set of numerical models. Beyond the steep scaling with $\alpha_{\text{eff}} \simeq 3/2$, our numerical calculations show a transition to a shallower heat transfer scaling at larger supercriticality \widetilde{Ra} . The characterisation of the upper bound of the rotation-dominated regime of rotating convection has been a long-standing question. The ratio of the global-scale Coriolis and buoyancy forces, approximated by the value of Ro_c , has long been postulated to control the transition from rotation-dominated convection to non-rotating convection (e.g. Gilman 1977; Zhong & Ahlers 2010; Stevens *et al.* 2013). Using a combination of laboratory experiments and local numerical simulations in cartesian coordinates, King *et al.* (2009) however demonstrated that a simple Ro_c criterion does not correctly capture the regime transition, which happens while the bulk Rossby number is still much smaller than unity (see also Cheng *et al.* 2015). They instead suggested that this transition is controlled by the competing thickness of the thermal and Ekman boundary layers. The resulting crossover was found to follow $RaE^{3/2} \sim 1$ (King *et al.* 2012). However, numerical experiments that employed stress-free boundary conditions, in which viscous boundary layers are not present, yield a similar regime transition, which questions the role of the Ekman layer on the regime change (e.g. Schmitz & Tilgner 2009).

Julien *et al.* (2012b) thus argued that the transition from *rotationally-constrained* to what they call *rotationally-influenced* convection is rather controlled by the dynamics of the thermal boundary layers. In particular, they proposed that the diffusion-free scaling (1.1) breaks down when the thermal boundary layer is no longer in geostrophic balance. In other words, $Nu \sim \widetilde{Ra}^{3/2}$ would hold as long as the local convective Rossby number in the thermal boundary layer Ro_λ remains smaller than unity. The definition of Ro_λ leads to

$$Ro_\lambda = \frac{Ra_\lambda^{1/2} E_\lambda}{Pr^{1/2}} = \frac{(\alpha_T g \Delta T_\lambda)^{1/2}}{\Omega \lambda^{1/2}},$$

where λ is the thermal boundary layer thickness. Since

$$Nu \sim \frac{\Delta T_\lambda}{\lambda} \frac{L}{\Delta T},$$

using (1.1), $Ro_\lambda \sim 1$ thus yields

$$Ra E^{8/5} Pr^{-3/5} \sim 1. \quad (3.7)$$

To test the applicability of this transition parameter, figure 7 shows the heat transfer data normalised by the diffusivity-free scaling (1.1), $Nu Ra^{-3/2} E^{-2}$, versus $Ra E^{8/5}$ for

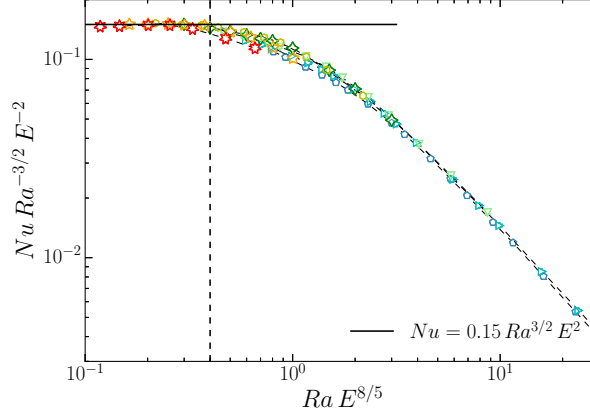


FIGURE 7. Nusselt number compensated by $Ra^{3/2}E^2$ as a function of $RaE^{8/5}$. Only the cases with $E \leq 3 \times 10^{-4}$ and $Nu \geq 2$ are displayed in this figure. The solid black line corresponds to the diffusivity-free scaling $Nu = 0.15 Ra^{3/2}E^2$ (Equation 3.8) already displayed in figure (5), while the vertical line corresponds to the dynamical boundary scaling $RaE^{8/5} = 0.4$. The symbols have the same meaning as in figure 1.

the numerical models with $E \leq 3 \times 10^{-4}$ and $Nu \geq 2$. The numerical simulations that fulfill $RaE^{8/5} < 0.4$ lie very close to the geostrophic scaling (1.1). A best fit to the 16 cases that satisfy this criterion indeed yields $NuRa^{-3/2}E^{-2} = 0.149(\pm 0.002)$. The combination of the two criteria $RaE^{4/3} > 6$ and $RaE^{8/5} < 0.4$ defines a wedge in the parameter space highlighted by the two black lines visible in figure 6 where the scaling

$$Nu = 0.149(\pm 0.002)Ra^{3/2}E^2 \quad (3.8)$$

holds. The transition parameter (3.7) introduced by Julien *et al.* (2012b) thus enables us to successfully demarcate the rotation-dominated regime and to efficiently collapse the heat transfer data across the regime transition.

3.2.2. Reynolds number scaling

To establish a scaling relation for the typical convective flow speed Re_c , we examine first the variations of the viscous dissipation rate ϵ_U . In the limit of vanishing Ekman number, the viscous dissipation is expected to primarily occur in the bulk of the fluid (Busse 1970). However, in the parameter range currently accessible to numerical models (i.e. $E \geq \mathcal{O}(10^{-7})$), dissipation by friction through the Ekman boundary layers might still contribute substantially to the total viscous dissipation rate (e.g. Aubert *et al.* 2001). We thus follow the same strategy that has been fruitfully introduced by Grossmann & Lohse (2000) for non-rotating RBC and decompose the viscous dissipation rate into a fluid bulk contribution ϵ_U^{bu} and a boundary layer contribution ϵ_U^{bl} :

$$\epsilon_U = \epsilon_U^{bu} + \epsilon_U^{bl} = \frac{\nu}{V} \left(\int_{\mathcal{T}} (\nabla \times \mathbf{u})^2 dV + \int_{V \setminus \mathcal{T}} (\nabla \times \mathbf{u})^2 dV \right), \quad (3.9)$$

where the integration domain is defined by $\mathcal{T} = \{r_i + \lambda_U^i \leq r \leq r_o - \lambda_U^o; 0 \leq \theta \leq \pi; 0 \leq \phi \leq 2\pi\}$, where λ_U^i (λ_U^o) are the thicknesses of the inner (outer) viscous boundary layer. We then establish scaling relations for the two contributions ϵ_U^{bu} and ϵ_U^{bl} as functions of Re_c and E , starting with the kinetic dissipation rate in the bulk of the fluid which can

be estimated by

$$\epsilon_U^{bu} \sim \nu \frac{U_c^2}{\ell_{\text{diss}}^2},$$

where ℓ_{diss} is the viscous dissipation length scale defined such that the local Reynolds number associated with this length scale is unity, i.e. $u_{\text{diss}} \ell_{\text{diss}} / \nu \sim 1$. Following [Davidson \(2013\)](#), we also introduce a small-scale vorticity ω_{diss} defined by $\omega_{\text{diss}} \sim u_{\text{diss}} / \ell_{\text{diss}}$, which yields

$$\epsilon_U^{bu} \sim U_c^2 \omega_{\text{diss}}. \quad (3.10)$$

At this stage, the study of the viscous dissipation rate needs to be complemented by a force balance analysis in order to estimate the scaling of ω_{diss} . A viscosity-free scaling of rotating convection was first proposed by [Stevenson \(1979\)](#) and [Ingersoll & Pollard \(1982\)](#) and later further developed by [Aubert *et al.* \(2001\)](#). This scaling, known as the inertial scaling of rapidly-rotating convection, hypothesises a triple force balance between Coriolis, inertia and Archimedean force (hereafter CIA). Taking the curl of the Navier-Stokes equation (2.2) in its dimensional form, the CIA triple balance yields

$$\Omega \frac{\partial \mathbf{u}}{\partial z} \sim \mathbf{u} \cdot \nabla \boldsymbol{\omega} \sim \nabla \times (\alpha_T T g \mathbf{e}_r),$$

where the factor two in the vortex stretching term has been omitted. We now introduce the two integral length scales ℓ_{\perp} and ℓ_{\parallel} , respectively perpendicular and parallel to the rotation axis. Since rapidly-rotating convective patterns take the form of columnar structures aligned with the rotation axis, $\ell_{\perp} \ll \ell_{\parallel}$. Denoting U_c the typical velocity, Θ the typical thermal perturbation and ω_c the typical vorticity, one gets

$$\Omega \frac{U_c}{\ell_{\parallel}} \sim U_c \frac{\omega_c}{\ell_{\perp}} \sim \alpha_T g \frac{\Theta}{\ell_{\perp}}. \quad (3.11)$$

We now assume that the axial dimension of the convection rolls ℓ_{\parallel} can be approximated by the container length scale L . This assumption combined with the balance between Coriolis force and inertia in (3.11) yields

$$\ell_{\perp} / L \sim \omega_c / \Omega. \quad (3.12)$$

We further assume that the convective heat flux per unit area \mathcal{Q} scales as

$$\mathcal{Q} \sim \rho c_p U_c \Theta \sim (Nu - 1) \kappa \rho c_p \Delta T / L,$$

which implies that the correlation between thermal perturbation and velocity are independent of E , Pr and Ra ([Gillet & Jones 2006](#)). The balance between inertia and buoyancy in (3.11) then leads to

$$Ra \mathcal{Q} Pr^{-2} \sim (L^4 / \nu^3) U_c^2 \omega_c.$$

Since on time average $(\nu^3 / L^4) \epsilon_U \sim Ra \mathcal{Q} Pr^{-2}$, it follows from (3.10) $\omega_{\text{diss}} \sim \omega_c$. The proportionality relation between the typical time scale at the integral length ℓ_{\perp} and at the dissipation scale ℓ_{diss} is a distinctive feature of two-dimensional turbulence (e.g. [Davidson 2015](#)). Finally assuming that $\omega_c \sim U_c / \ell_{\perp}$, one can derive the following expression for the viscous dissipation rate in the fluid bulk

$$\epsilon_U^{bu} = \frac{U_c^3}{\ell_{\perp}} = \frac{\nu^3}{L^4} \frac{Re_c^{5/2}}{E^{1/2}}. \quad (3.13)$$

The same procedure can be applied to the viscous dissipation in the Ekman boundary layers with the difference that the typical length scale is now the boundary layer thickness

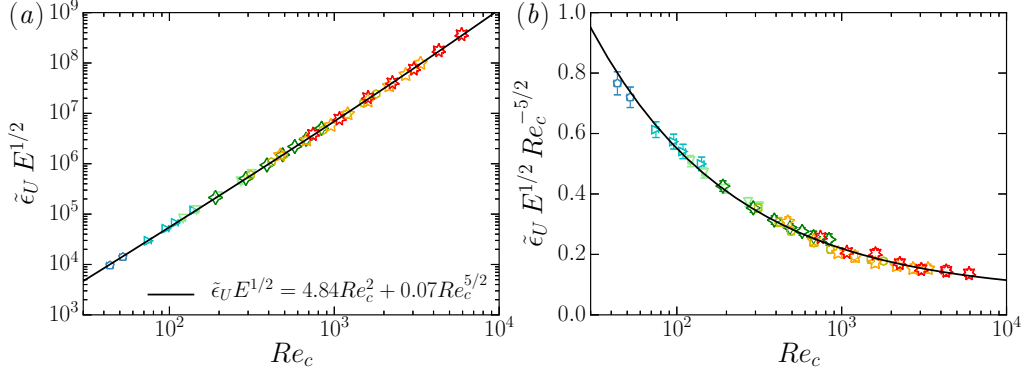


FIGURE 8. (a) Dimensionless viscous dissipation rate $\tilde{\epsilon}_U$ as a function of the Reynolds number Re_c . (b) Corresponding compensated $\tilde{\epsilon}_U$ scaling. The solid black lines correspond to the theoretical scaling derived in (3.15) with $a = 0.066$ and $b = 4.843$. Only the cases that fulfill the conditions $Nu > 2$ and $RaE^{8/5} < 1$ have been selected on this figure. The error bars illustrate the r.m.s. fluctuations and correspond to one standard-deviation from the time-averages. The symbols have the same meaning as in figure 1.

λ_U . Furthermore, the dissipation occurs only in the fraction of the fluid volume occupied by the viscous boundary layers. In the limit of $\lambda_U \ll L$, this volume fraction can be approximated by the ratio λ_U/L , thus neglecting any curvature effect. This yields

$$\epsilon_U^{bl} \sim \nu \frac{U_c^2}{\lambda_U^2} \frac{\lambda_U}{L}.$$

Since $\lambda_U/L \sim E^{1/2}$ (see below in § 3.2.5), the viscous dissipation by friction through the boundary layers can be expressed by

$$\epsilon_U^{bl} \sim \frac{\nu^3}{L^4} \frac{Re_c^2}{E^{1/2}}. \quad (3.14)$$

Combining the equations (3.13) and (3.14) allows us to derive the following scaling behaviour for the dimensionless viscous dissipation rate

$$\tilde{\epsilon}_U = a \frac{Re_c^{5/2}}{E^{1/2}} + b \frac{Re_c^2}{E^{1/2}}. \quad (3.15)$$

To test the validity of this scaling, we calculate $\tilde{\epsilon}_U$ and Re_c in our numerical simulations and directly fit the expression (3.15). This leaves only the two prefactors a and b as free fitting parameters. Figure 8(a) shows $\tilde{\epsilon}_U E^{1/2}$ as a function of Re_c for the 41 cases that fulfill $Nu > 2$ and $RaE^{8/5} < 1$. The best-fit to the numerical data yields $a = 0.066(\pm 0.003)$ and $b = 4.843(\pm 0.096)$. The expression (3.15) provides an excellent agreement with the data, further confirmed by the bulk compensated scaling $\tilde{\epsilon}_U E^{1/2} Re_c^{-5/2}$ shown in panel (b). Explicitly including the viscous friction that occurs in the Ekman boundary layers thus allows to very accurately describe the numerical data over a broad range of parameter $3 \times 10^{-4} \leq E \leq 3 \times 10^{-7}$, $10^2 \leq Re_c \leq 10^4$. We also note that a stricter restriction to the 16 turbulent cases that satisfy the criterion $RaE^{8/5} < 0.4$ and thus lie within the wedge displayed in figure (6) yields very similar values for a and b . The expression (3.15) also allows to estimate the transition value of Re_c beyond which the viscous dissipation that occurs in the interior of the fluid will dominate the dissipation in boundary layers. Figure 8(b) demonstrates that our dataset nearly reaches this point where the bulk scaling alone provides a good description. Using the best fitting parameters a and b yields

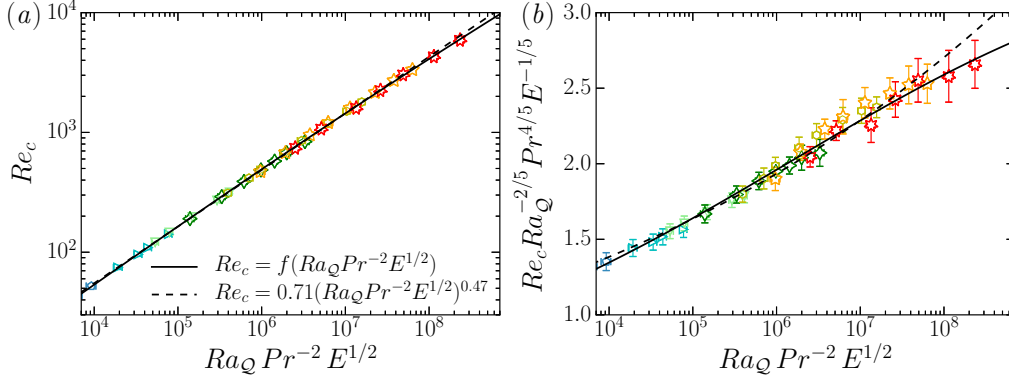


FIGURE 9. (a) Reynolds number Re_c as a function of $Ra_Q Pr^{-2} E^{1/2}$. (b) Corresponding compensated Re_c scaling. The solid black lines correspond to the theoretical scaling derived in (3.19), while the dashed black lines correspond to the least-square fit to the data. Only the cases that fulfill the conditions $Nu > 2$ and $RaE^{8/5} < 1$ have been selected on this figure. The error bars illustrate the r.m.s. fluctuations and correspond to one standard-deviation from the time-averages. The symbols have the same meaning as in figure 1.

$Re_c = (b/a)^2 \simeq 5500$. Beyond this value, the viscous dissipation in the Ekman layers becomes secondary and the dynamical behaviour will then gradually tend towards the inertial scaling of rotating convection.

Assuming that the viscous dissipation either entirely occurs in the fluid bulk (i.e. $\epsilon_U \simeq \epsilon_U^{bu}$) or in the Ekman layers (i.e. $\epsilon_U \simeq \epsilon_U^{bl}$) allows to define the two end-member scaling relations:

$$Re_c^{bu} \leq Re_c \leq Re_c^{bl}, \quad (3.16)$$

where

$$Re_c^{bl} \sim Ra_Q^{1/2} Pr^{-1} E^{1/4} \quad (3.17)$$

and

$$Re_c^{bu} \sim Ra_Q^{2/5} Pr^{-4/5} E^{1/5}. \quad (3.18)$$

We note that (3.18) corresponds to the convective velocity scaling classically obtained in the CIA triple balance (e.g. Aubert *et al.* 2001; Gillet & Jones 2006; Barker *et al.* 2014), while the scaling (3.17) has the same dependence on Ra_Q as the VAC triple balance (3.5) but carries a different E -scaling exponent. Once a and b have been determined, the equation (3.15) can be numerically solved to derive the combined scaling law for Re_c :

$$Re_c = f(Ra_Q Pr^{-2} E^{1/2}). \quad (3.19)$$

For comparison purposes, we also compute a simple best fit to the data which yields $Re_c = 0.708(\pm 0.017)(Ra_Q Pr^{-2} E^{1/2})^{0.473 \pm 0.002}$. Figure 9(a) shows Re_c versus $Ra_Q Pr^{-2} E^{1/2}$ for the 41 cases already shown in figure 8, while figure 9(b) shows the corresponding bulk compensated scaling.

Previous parameter studies of rotating convection in spherical shells either carried out under the quasi-geostrophic assumption (Gillet & Jones 2006; Guervilly 2010) or in fully three-dimensional models (Christensen 2002; King & Buffett 2013) obtained steeper exponents than the 2/5 scaling expected in the classical CIA balance (Equation 3.18). This discrepancy has usually been attributed to the significant role played by viscosity in numerical models and thus prompted several authors to rather describe their dataset using the VAC scaling hypothesis (3.5). Since the scaling exponents are

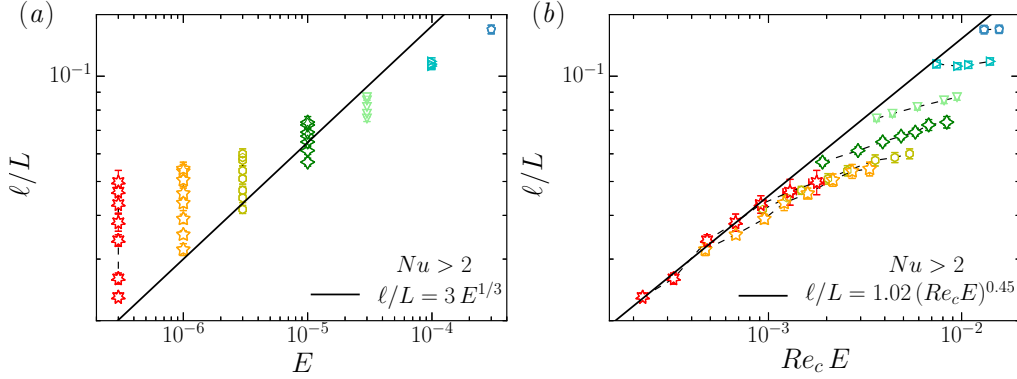


FIGURE 10. (a) Average flow length scale ℓ/L calculated using (2.10) as a function of the Ekman number for the numerical models with $E \leq 3 \times 10^{-4}$ and $Nu > 2$. For comparison, the weakly non-linear scaling obtained in figure 4 has been plotted as a solid black line. (b) Corresponding compensated ℓ/L scaling. Only the 41 cases that satisfy $Nu > 2$ and $Ra E^{8/5} < 1$ have been selected on this figure. The solid black line corresponds to the best-fit to the cases with $E = 3 \times 10^{-7}$. The error bars illustrate the r.m.s. fluctuations and correspond to one standard-deviation from the time-averages. The symbols have the same meaning as in figure 1.

relatively close to each other, $2/5$ versus $1/2$ regarding the dependence on Ra_Q^\dagger , discriminating one scaling from another remains however a difficult task (King & Buffett 2013). Here we show that the separation of ϵ_U into boundary layers and bulk contributions allows to very accurately describe the numerical data. Moreover, in the range of Re_c covered by our numerical dataset (i.e. $10^2 \leq Re_c < 10^4$), the simple power law $Re_c = 0.708(\pm 0.017)(Ra_Q Pr^{-2} E^{1/2})^{0.473 \pm 0.002}$ provides a statistically nearly indiscernible fit quality from the scaling theory (3.19). Deviations only become more significant at the high-end of the parameter range, where the power law fails to accurately capture the complex dependence of Re_c upon $Ra_Q Pr^{-2} E^{1/2}$. This explains why previous analyses that reduced the scaling behaviours of Re_c to such simple power laws obtained scaling exponents robustly larger than $2/5$ (e.g. Gillet & Jones 2006; King & Buffett 2013).

3.2.3. Flow length scales and interior temperature gradients

Using the equations (3.12) and (3.18), the inertial theory of rotating convection predicts the following scaling for the integral flow length scale ℓ_\perp

$$\ell_\perp/L \sim (U_c/\Omega L)^{1/2} \sim (Re_c E)^{1/2}, \quad (3.20)$$

which is generally referred to as the Rhines scaling (Rhines 1975). Using the numerical models computed by Christensen & Aubert (2006), several analyses of the typical flow length scale suggest that the VAC scaling (3.4) might possibly hold beyond the weakly non-linear regime of rotating convection (e.g. King & Buffett 2013; Oruba & Dormy 2014). Figure 10(a) shows the calculations of the average flow length scale ℓ/L plotted as a function of E for the numerical models with $E \leq 3 \times 10^{-4}$ and $Nu > 2$. The $\ell \sim E^{1/3} L$ scaling that accurately describes the numerical data close to onset of convection (see figure 10) fails to properly capture the length scale variations in the non-linear regime. Especially, at low Ekman numbers ($E \leq 3 \times 10^{-6}$), ℓ exhibits a strong additional dependence on the convective forcing and increases with the supercriticality (see Table A1 for details). Figure 10(b) shows the calculations of ℓ versus $Re_c E$ for the 41 numerical models already shown in figures 8 and 9. A best-fit to the cases with $E = 3 \times 10^{-7}$ that

[†] Note however that the Ekman number dependence is not the same for these two scalings.

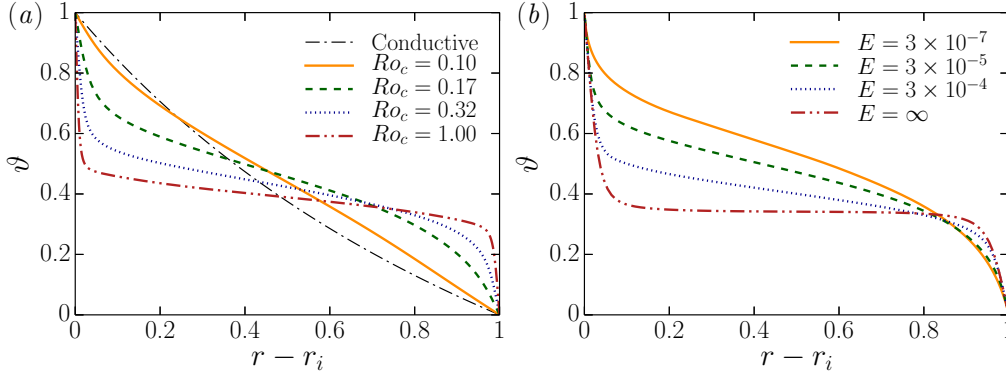


FIGURE 11. (a) Radial profile of the time and horizontally-averaged temperature $\vartheta(r)$ for different convective Rossby number Ro_c with a fixed Ekman number of $E = 10^{-4}$. The dash-dotted black line corresponds to the conductive temperature profile solution of (2.7). (b) Radial profile of the time and horizontally-averaged temperature $\vartheta(r)$ for different Ekman numbers with approximately the same Nusselt number $10.3 < Nu < 11$.

fulfill $RaE^{8/5} < 0.4$ yields $\ell/L = 1.016(\pm 0.212)(Re_c E)^{0.45(\pm 0.027)}$, reasonably close to the theoretical scaling (3.20). Since the dissipation that occurs in the boundary layers still plays a substantial role in the velocity scaling (3.15), it is not surprising that (3.20) is only approached for the lowest Ekman number considered in this study.

While non-rotating convection undergoes an efficient turbulent mixing which results in an isothermal fluid interior (e.g. Vericco & Camussi 1999), the prominent role played by the Coriolis force in rotating convection impedes the mixing. Both experiments (e.g. Boubnov & Golitsyn 1990; Kunnen *et al.* 2010) and direct numerical simulations (e.g. Julien *et al.* 1996; King *et al.* 2012; Stellmach *et al.* 2014) have indeed revealed that a large-scale interior temperature gradient can be maintained in the rapidly-rotating regime (see also Gillet & Jones 2006; King *et al.* 2010). Figure 11 shows the time and horizontally averaged temperature profile $\vartheta(r)$ for several rotating and non-rotating models. At a fixed Ekman number, an increase of the supercriticality (panel a) changes the temperature distribution from a nearly conductive state (solid orange line) to a nearly isothermal fluid bulk (dot-dashed line). At larger Ro_c (broken lines), the rotational constraint decreases and thin thermal boundary layers start to emerge and tend to accommodate an increasing fraction of the temperature drop. As visible on panel (b), the transition from rotating to non-rotating convection is thus associated with a gradual lowering of the average temperature gradient and a transition to a physical regime where boundary layers entirely control the heat transfer.

Measuring the interior temperature gradient β_T (2.9) thus helps to characterise the heat transfer regime. Figure 12(a) shows β_T versus \widetilde{Ra} for the set of numerical simulations with $E \leq 10^{-3}$. An increase of the supercriticality \widetilde{Ra} leads to a gradual decrease of $|\beta_T|$. The thermal profiles in the fluid bulk tend to a thermally well-mixed interior (i.e. vanishing β_T) when the rotational influence on the flow decreases. In contrast to the asymptotic calculations by Julien *et al.* (2012b), our dataset does not show any evidence for a direct scaling relation between β_T and \widetilde{Ra} . However, following Stevenson (1979) and Barker *et al.* (2014), the interior temperature gradient can be estimated by

$$\beta_T \sim \frac{\Theta}{\ell_{\perp}} \frac{L}{\Delta T},$$

in the rapidly-rotating limit. Using (3.20) for the length scale scaling and approximating

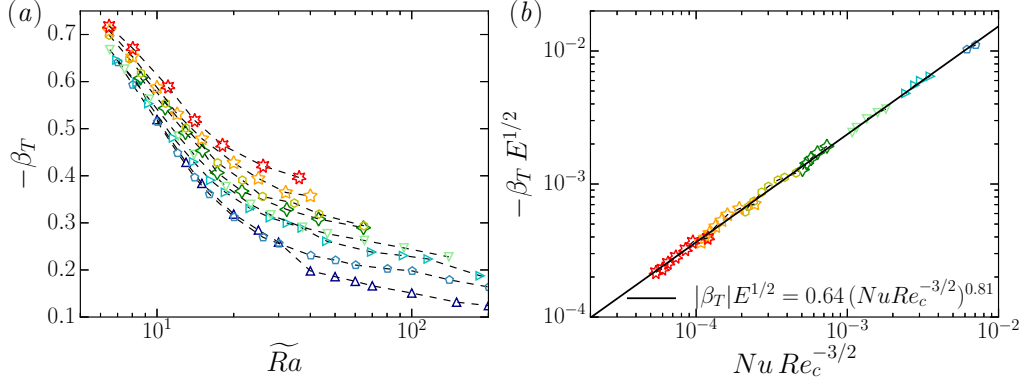


FIGURE 12. (a) Temperature gradient at mid-shell radius β_T versus \widetilde{Ra} for the numerical models with $Nu > 2$ and $E \leq 10^{-3}$. (b) Absolute temperature gradient at mid-shell renormalised by $E^{-1/2}$ versus $Nu Re_c^{-3/2}$ for the numerical models with $Ra E^{8/5} < 1$ and $Nu > 2$. The solid black line corresponds to the best-fit to the data. The symbols have the same meaning as in figure 1.

$\Theta/\Delta T$ by Nu/Re_c then yields

$$\beta_T \sim Nu Re_c^{-3/2} E^{-1/2}. \quad (3.21)$$

Figure 12(b) shows that this scaling provides a reasonable description of the 41 numerical cases already discussed in figures 8 and 9. The best-fit to the data however gives a shallower exponent than expected from theory: $\beta_T E^{1/2} = 0.643(\pm 0.027)(Nu Re_c^{-3/2})^{0.812(\pm 0.005)}$. This discrepancy is not surprising since the underlying ℓ_\perp scaling that enters (3.21) is only partially realised in our set of simulations (see figure 10). Lowering the Ekman number further might help to ascertain this scaling. Indeed, the local numerical calculations carried out in cartesian coordinates by Barker *et al.* (2014) demonstrates the validity of (3.21) once the influence of the viscous boundary layers has been minimised. Replacing the expected asymptotic scalings for Nu (Equation 1.1) and Re_c (Equation 3.18) in (3.21) yields $\beta_T \sim Pr$. This implies that β_T should saturate on a constant value in the turbulent quasi-geostrophic regime of rotating convection. Local numerical calculations carried out in cartesian coordinates by Stellmach *et al.* (2014) indeed obtain a saturation of β_T for $E = \mathcal{O}(10^{-7})$ and $\widetilde{Ra} \sim 100$.

3.2.4. Thermal boundary layers

Since the heat transport in the thermal boundary layers is controlled by diffusion, the Nusselt number provides an estimate for the ratio between the thermal boundary layer thickness and the related temperature drop:

$$Nu = \eta \frac{\Delta T_i}{\lambda_T^i} \frac{L}{\Delta T} = \frac{1}{\eta} \frac{\Delta T_o}{\lambda_T^o} \frac{L}{\Delta T},$$

where λ_T^i (λ_T^o) is the thickness of the thermal boundary layer at the inner (outer) boundary and ΔT_i (ΔT_o) is the associated temperature contrast. This yields the following scalings for the thermal boundary layer thicknesses at both boundaries:

$$\frac{\lambda_T^i}{L} = \eta \frac{\Delta T_i}{\Delta T} \frac{1}{Nu}; \quad \frac{\lambda_T^o}{L} = \frac{1}{\eta} \frac{\Delta T_o}{\Delta T} \frac{1}{Nu}. \quad (3.22)$$

In non-rotating convection in spherical geometry, the thermal boundary layer are asymmetric and thus $\Delta T^i/\Delta T^o \neq 1$. In a previous study, we demonstrated that the ratio

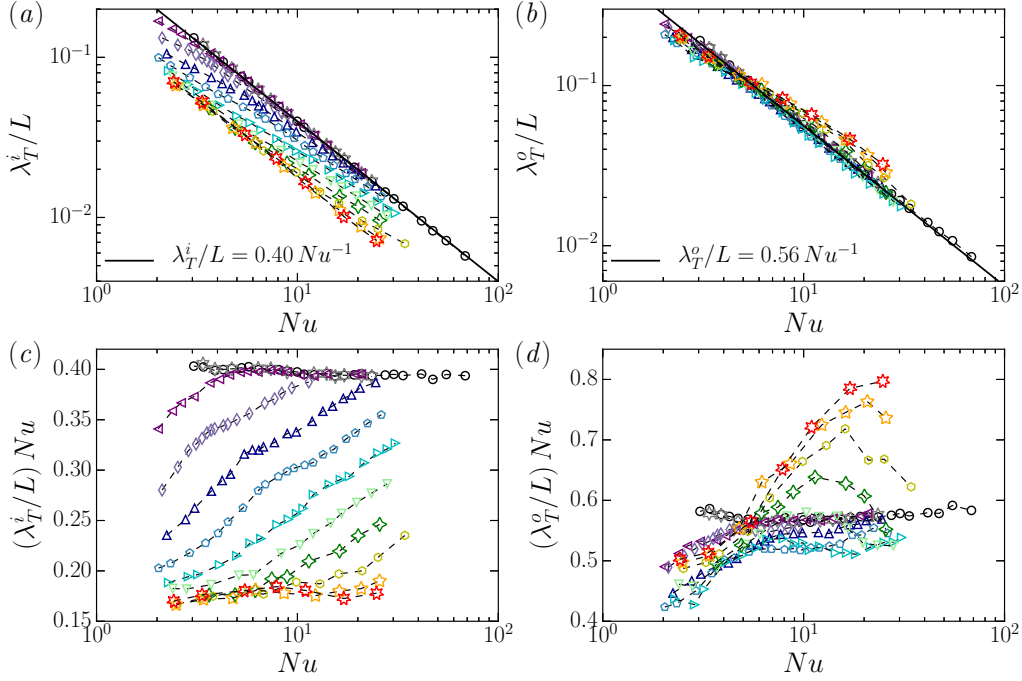


FIGURE 13. (a,b) Thermal boundary layer thickness at the inner (outer) boundary λ_T^i (λ_T^o) as a function of the Nusselt number. The solid black lines correspond to the theoretical scalings for non-rotating convection derived in (Gastine *et al.* 2015). (c,d) Compensated λ_T^i/L (λ_T^o/L) scaling. The symbols have the same meaning as in figure 1.

$\Delta T^i/\Delta T^o$ only depends on the radius ratio η and on the gravity profile $\tilde{g}(r)$ (Gastine *et al.* 2015). Thus, the scaling for the boundary layer thickness in non-rotating RBC is

$$\lambda_T^i/L \sim \lambda_T^o/L \sim Nu^{-1}. \quad (3.23)$$

where only the scaling prefactors depend on the geometry and on the gravity distribution of the spherical shell. In rotating convection however, the temperature drops at each thermal boundary layer are likely to also depend on Ra and E and hence a non trivial additional dependence on Nu might be expected (see figure 11). Figure 13 shows the calculations of λ_T^i and λ_T^o using the slope-intersection method described in § 2.3 versus Nu for both rotating and non-rotating simulations. As pointed out by Julien *et al.* (2012b), other methods to estimate the thermal boundary layers in rotating convection might yield different thicknesses. A comparison between the values obtained from the slope intersection method with the location of the peaks of the r.m.s. of the temperature fluctuations for a few selected cases however yield similar boundary layer thicknesses (for a comparison, see Gastine *et al.* 2015). Large Ekman number models ($E \geq 10^{-2}$) essentially behave similarly to the non-rotating cases. At the inner boundary of the spherical shell, the cases with intermediate Ekman numbers $3 \times 10^{-5} \leq E \leq 3 \times 10^{-3}$ exhibit a lower prefactor and a slightly shallower slope than Nu^{-1} particularly visible in the compensated plot displayed in panel (c). The cases with $E \leq 3 \times 10^{-6}$, however seem to follow again a scaling $\lambda_T^i/L \sim Nu^{-1}$, though with a much smaller prefactor ($\simeq 0.17$ instead of $\simeq 0.4$) than the non-rotating cases. The thermal boundary layer at the outer boundary behaves quite differently. On average, λ_T^o remains much closer to the values found in the non-rotating models and can thus be roughly approximated

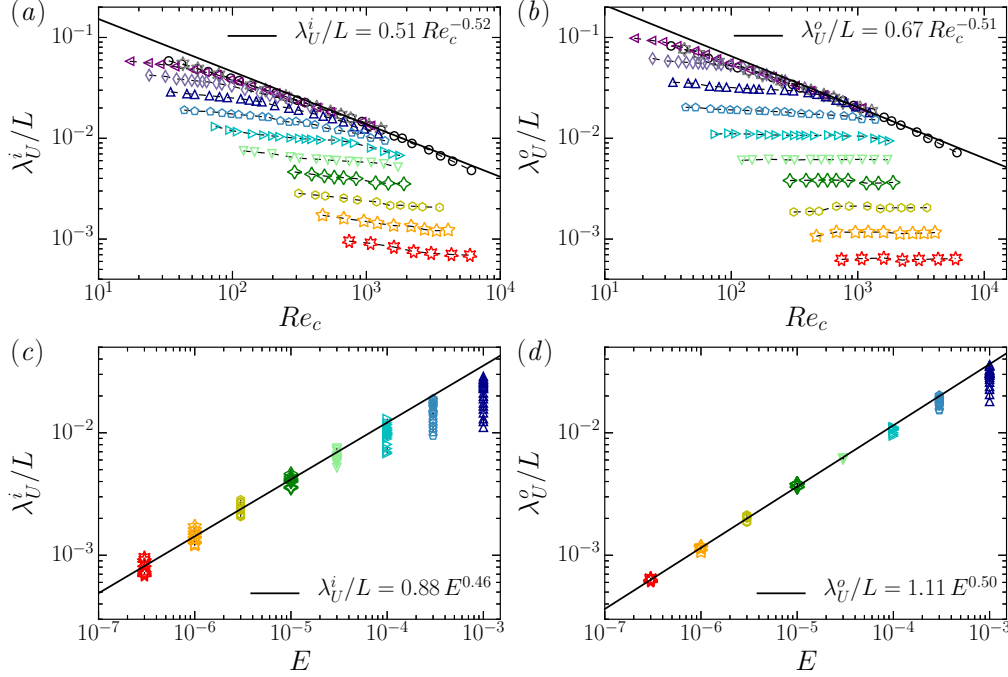


FIGURE 14. (a,b) Viscous boundary layer thickness at the inner (outer) boundary λ_U^i (λ_U^o) as a function of Re_c . The solid lines correspond to the scalings obtained for non-rotating convection derived in (Gastine *et al.* 2015). (c,d) Viscous boundary layer thickness at the inner (outer) boundary as a function of the Ekman number. The solid black lines correspond to the best-fit to the 41 cases that fulfill $RaE^{8/5} < 1$ and $Nu > 2$. The symbols have the same meaning as in figure 1.

by $\lambda_T^o/L \sim Nu^{-1}$. However, a secondary, intricate dependence on the Ekman number remains, as visible on the compensated scaling of λ_T^o displayed in panel (d). For both boundary layers, the Nu^{-1} scaling thus provides an acceptable first-order approximation of the thermal boundary layer thickness measured by the slope intersection method, though subtle dependences on the Ekman number can impinge on both the prefactor and the scaling exponent.

3.2.5. Viscous boundary layers

In the range of Rayleigh numbers explored here ($10^3 \leq Ra \leq 10^{11}$), the viscous boundary layers in non-rotating convection are usually assumed to be laminar and follow the Prandtl-Blasius boundary layer theory (Prandtl 1905; Blasius 1908). Balancing the inertia of the fluid bulk with the viscous forces in the boundary layers yields

$$\lambda_U/L \sim Re^{-1/2}. \quad (3.24)$$

In contrast, owing to the primary role of Coriolis force, the viscous boundary layers in rotating convection, called the Ekman layers, differ greatly from non-rotating convection. A scaling relation for the Ekman layers can be derived by considering a force balance between Coriolis force and viscosity in the limit of $E \rightarrow 0$ (e.g. Greenspan 1968):

$$\Omega \times \mathbf{u} \sim \nu \Delta \mathbf{u} \quad \rightarrow \quad \lambda_U/L \sim E^{1/2}. \quad (3.25)$$

Figure 14 shows the calculations of the viscous boundary layer thicknesses for both the inner and the outer spherical shell boundaries as a function of Re_c and E . Here we only

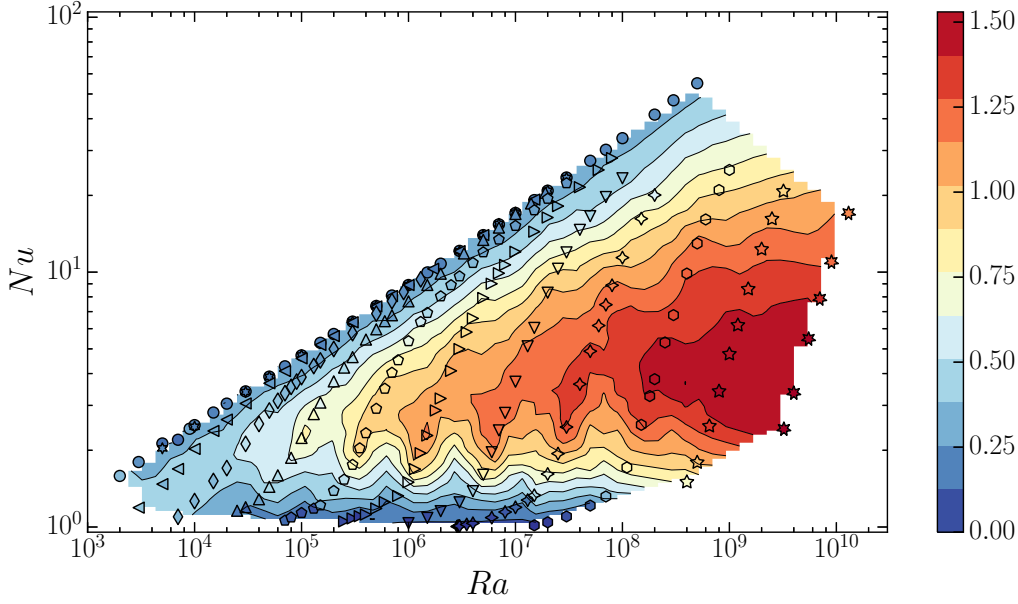


FIGURE 15. Isocontours of the local effective exponent α_{eff} of the $Nu = Ra^{\alpha_{\text{eff}}} E^{\beta_{\text{eff}}}$ scaling in the (Ra, Nu) -plane. The symbol shape corresponds to the Ekman number as in the previous figures, while the symbol color scales here with the value of local slope α_{eff} .

examine the mean viscous boundary layer, though in spherical geometry the Ekman layer thickness might also depend on the latitude (Greenspan 1968). When the Ekman number is large ($E \geq 3 \times 10^{-3}$), the influence of rotation on the viscous boundary layer remains secondary. λ_U^i and λ_U^o are then essentially the same as the non-rotating cases (panels *a* and *b*). As already shown in our previous study (Gastine *et al.* 2015), when $Re_c \geq 250$, the scaling exponents are in close agreement with the Prandtl-Blasius scaling (3.24). At lower Ekman numbers ($E \leq 3 \times 10^{-5}$), the viscous boundary layer thicknesses become almost independent of Re_c and approach the theoretical scaling for Ekman layers (panels *c* and *d*). Indeed, the best-fit to the numerical cases that fulfill $RaE^{8/5} < 1$ and $Nu > 2$ yields $\lambda_U^i/L = 0.875(\pm 0.084) E^{0.465(\pm 0.008)}$ and $\lambda_U^o/L = 1.109(\pm 0.042) E^{0.497(\pm 0.003)}$, in good agreement with (3.25).

3.3. Transitional regime: from rotating to non-rotating convection

In the previous sections, we mainly explored the range of parameters where the convective flow is strongly constrained by rotation. We showed that the criterion $RaE^{8/5} \leq \mathcal{O}(1)$ posited by Julien *et al.* (2012a) provides an effective way to characterise the upper bound of this physical regime. Beyond this point, i.e. when $Ra > E^{-8/5}$, convection is still influenced by rotation but does no longer operate in the turbulent quasi-geostrophic regime. This defines the lower bound of the *transitional regime* of rotating convection. To illustrate the continuous variations of the physical properties within this regime, figure 15 shows isocontours of the local slope α_{eff} of the Nusselt scaling in a (Ra, Nu) -plane. Beyond the rapidly-rotating regime of convection in which $\alpha_{\text{eff}} \simeq 3/2$ (dark red area), a rapid decrease of the local exponent is observed. The heat transport is not characterised by one single scaling exponent α_{eff} but rather exhibits continuous changes, similarly to what is observed in classical RBC (e.g. Grossmann & Lohse 2000; Funfschilling *et al.* 2005). In addition, Nu does not follow a pure function of the supercriticality \bar{Ra} any longer

and the local variations of β_{eff} thus decorrelate from those of α_{eff} (see figure 5). The numerical models with higher E and Ra in which the influence of Coriolis force becomes negligible then transition to a slow growth of Nu with Ra close to the values obtained in non-rotating convection (i.e. $\alpha_{\text{eff}} < 0.4$, $\beta_{\text{eff}} \simeq 0$). This defines the upper bound of the transitional regime.

To determine a transition criterion that only depends on the control parameters, we hypothesise that the transition between rapidly-rotating and weakly-rotating convection can be defined as the intersection between the steep asymptotic diffusivity-free scaling for rotating convection (1.1) and the shallow scaling for non-rotating convection $Nu_{\text{NR}} \sim Ra^{\nu_{\text{eff}}}$. Following Cheng *et al.* (2015) we thus designate Ra_T for the upper bound of the transitional regime by

$$Ra_T \sim E^{-4/(3-2\nu_{\text{eff}})},$$

where the unconstrained Pr dependence has been dropped. Since the local slope for non-rotating heat transfer increases from roughly $\nu_{\text{eff}} = 0.27$ to $\nu_{\text{eff}} = 0.32$ between $Ra = 10^5$ and $Ra = 10^9$ in non-rotating spherical shells (Gastine *et al.* 2015), Ra_T can range from $E^{-1.62}$ to $E^{-1.69}$. In addition, the Grossmann & Lohse (2000) theory predicts a further increase of ν_{eff} beyond $Ra = 10^9$ to reach $\nu_{\text{eff}} = 1/3$ (Chillà & Schumacher 2012). We thus rather decide to adopt $Nu_{\text{NR}} \sim Ra^{1/3}$ as the physically-motivated asymptotic scaling for non-rotating convection. This yields

$$Ra_T \sim E^{-12/7}, \quad (3.26)$$

a value that lies within the range predicted by Ecke & Niemela (2014). The transitional regime of rotating convection thus covers the broad parameter range $E^{-8/5} \leq Ra \leq E^{-12/7}$ in which the flow properties will continuously vary to match the regime changes between rotation-dominated and non-rotating convection. Due to the intricate nature of the force balance with possible crossovers of leading forces, the derivation of asymptotic scalings inherent in this transitional regime is challenging. In the following, we thus rather check whether Ra_T (3.26) represents an accurate transition parameter that separates the regime of rotating convection from the gradual transition to non-rotating behaviour.

3.3.1. Nusselt and Reynolds numbers

Figure 16 shows the calculations of the Nusselt number compensated by the heat transfer scaling for non-rotating convection as a function of the transition parameter (3.26). In panel (a), Nu is compensated on the y -axis by the asymptotic scaling $Nu_{\text{NR}} \sim Ra^{1/3}$. Well into the rapidly-rotating regime (i.e. $RaE^{12/7} \ll 1$), the heat transfer follows the $Nu \sim Ra^{3/2}E^2$ scaling (solid line). The growth of $RaE^{12/7}$ is then accompanied by a lowering of the heat transfer slope which levels off around the non-rotating asymptotic scaling when $RaE^{12/7} \gg 1$ (dotted vertical line). Similarly to King *et al.* (2012), the data are more scattered in the weakly-rotating regime. This is expected since the asymptotic scaling $Nu_{\text{NR}} \sim Ra^{1/3}$ used to renormalise the data is not yet realised in the range of Rayleigh numbers covered by our numerical dataset. A much better collapse of the data can nevertheless be achieved by normalising Nu with the actual calculations of Nu_{NR} , the Nusselt numbers of the corresponding non-rotating simulations at the same Rayleigh numbers (panel b). Since a direct computation of the non-rotating models with $Ra > 10^9$ becomes numerically intractable, the scaling laws derived in Gastine *et al.* (2015) have been used to estimate Nu_{NR} for the cases with $Ra > 10^9$. This renormalisation allows to better describe the range $10 \leq RaE^{12/7} \leq 10^4$ and to remarkably collapse all the rotating simulations with $Nu > 2$ on one single curve.

We can check whether the regime transition criterion (3.26) also applies to the scalings

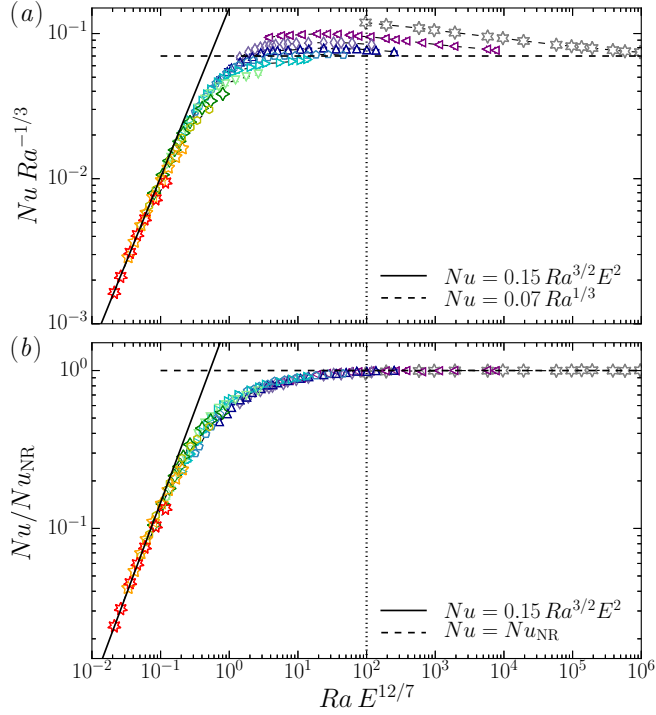


FIGURE 16. (a) Nusselt number Nu renormalised by $Ra^{1/3}$ as a function of $Ra E^{12/7}$ (Equation 3.26). The solid black line corresponds to the asymptotic scaling for rotating convection (3.8), while the dashed line corresponds to the tentative asymptotic scaling for non-rotating convection. (b) Nusselt number Nu renormalised by Nu_{NR} as a function of $Ra E^{12/7}$. Nu_{NR} corresponds to the Nusselt number of the non-rotating cases at the same Rayleigh number. On both panels, the weakly non-linear cases with $Nu < 2$ have been excluded. The dotted vertical lines correspond to the Rayleigh number $Ra = 100 E^{-12/7}$ beyond which Nu adopts a scaling behaviour close to the non-rotating RBC. The symbols have the same meaning as in figure 1.

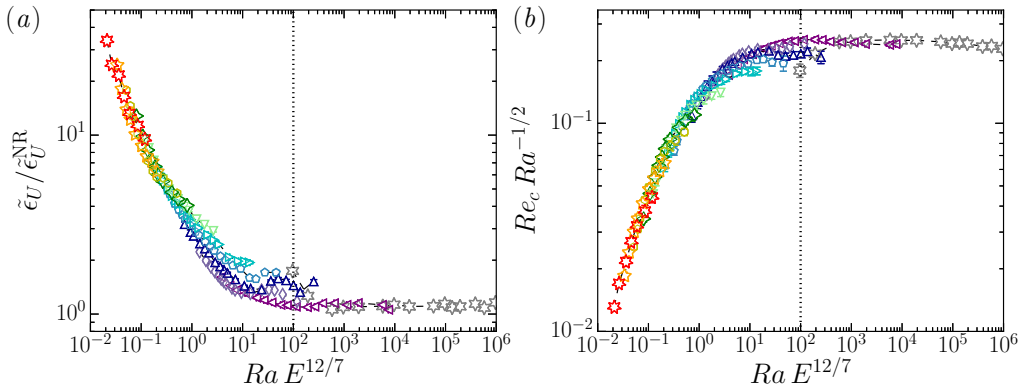


FIGURE 17. (a) Dimensionless viscous dissipation rate $\tilde{\epsilon}_U$ normalised by the scaling for the viscous dissipation rate obtained in non-rotating convection $\tilde{\epsilon}_U^{NR} = 7.08 Re_c^{5/2} + 0.25 Re_c^3$ (see Gastine *et al.* 2015) as a function of $Ra E^{12/7}$ (Equation 3.26). (b) Reynolds number Re_c renormalised by $Ra^{1/2}$ as a function of $Ra E^{12/7}$. On both panels, the weakly non-linear cases with $Nu < 2$ have been excluded. The dotted vertical lines correspond to the Rayleigh number $Ra = 100 E^{-12/7}$ beyond which $\tilde{\epsilon}_U$ and Re_c adopt scaling behaviours close to the non-rotating RBC. The symbols have the same meaning as in figure 1.

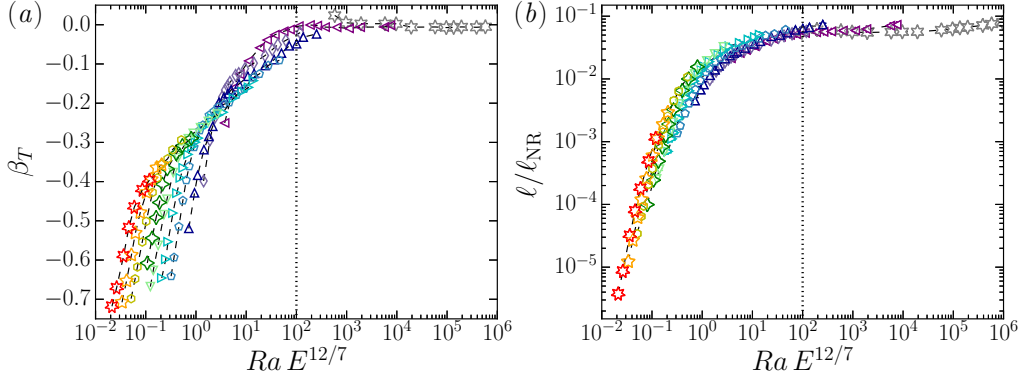


FIGURE 18. (a) Temperature gradient at mid-shell β_T as a function of $RaE^{12/7}$ (Equation 3.26). (b) Convective flow lengthscale ℓ normalised by the scaling for the plume spacing obtained in non-rotating convection ℓ_{NR} as a function of $RaE^{12/7}$ (Gastine *et al.* 2015). On both panels, the weakly non-linear cases with $Nu < 2$ have been excluded. The dotted vertical lines correspond to the Rayleigh number $Ra = 100 E^{-12/7}$ beyond which β_T and ℓ adopt scaling behaviours close to the non-rotating RBC. The symbols have the same meaning as in figure 1.

of the dimensionless viscous dissipation rate $\tilde{\epsilon}_U$ and of the flow speed Re_c . In non-rotating convection, $\tilde{\epsilon}_U$ can also be decomposed into fluid bulk and boundary layers contributions. Grossmann & Lohse (2000) predicted a scaling of the form $\tilde{\epsilon}_U^{NR} \sim a Re_c^3 + b Re_c^{5/2}$, which has been found to also accurately describe the numerical models of non-rotating convection in spherical shells (Gastine *et al.* 2015). Figure 17(a) thus shows $\tilde{\epsilon}_U$ renormalised by $\tilde{\epsilon}_U^{NR}$ found by Gastine *et al.* (2015) as a function of the transition parameter. In non-rotating convection, the dependence of the Reynolds number upon Ra cannot be simply reduced to a simple power law but rather exhibits continuous changes in the local slope exponent, analogous to the Nusselt number scaling. We thus follow the same procedure as for the Nusselt number and renormalise Re_c by the expected asymptotic scaling from the Grossmann & Lohse (2000) theory in the limit of large Ra , i.e. $Re_c^{NR} \sim Ra^{1/2}$. Figure 17(b) shows the calculations of $Re_c Ra^{-1/2}$ versus $RaE^{12/7}$. Except for the intermediate parameter range $1 \leq RaE^{12/7} \leq 10^2$, the numerical data for both $\tilde{\epsilon}_U$ and Re_c are well collapsed on a single curve. We note that the scatter of the data in panel (b) could be possibly further reduced by rather considering the actual values of Re_c^{NR} calculated in the non-rotating models. Beyond $RaE^{12/7} = \mathcal{O}(10^2)$ (dotted vertical lines), both $\tilde{\epsilon}_U$ and Re_c adopt scaling behaviours close to the classical non-rotating RBC.

3.3.2. Flow length scale and interior temperature gradient

We now turn to discussing the variations of the bulk temperature gradient β_T and average flow lengthscale ℓ across the regime transition from rotating to non-rotating convection. Figure 18(a) shows β_T as a function of $RaE^{12/7}$. In contrast to the previous quantities, we observe a significant scatter of the data in the rapidly-rotating regime. As discussed above and similarly to the findings by King *et al.* (2013), β_T depends on Ra and E in a complex fashion that is not captured by the transition parameter (3.26). In the weakly-rotating limit (i.e. $RaE^{12/7} > 10^2$), the bulk of the fluid becomes thermally well-mixed leading to $\beta_T \simeq 0$.

The study of the flow length scale necessitates the determination of an asymptotic scaling for ℓ in the non-rotating regime of convection. In classical RBC experiments with rigid sidewalls, the bulk flow is dominated by a large scale circulation (LSC) pattern. The average flow length scale can therefore be approximated by the vertical size of the

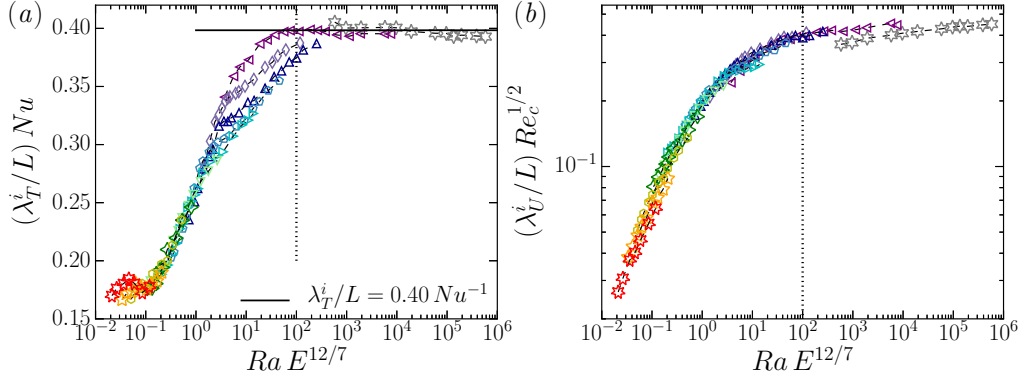


FIGURE 19. (a) Thermal boundary layer thickness at the inner boundary (λ_T^i) normalised by Nu^{-1} as a function of $RaE^{12/7}$ (Equation 3.26). The solid black line corresponds to the theoretical scaling obtained in [Gastine et al. \(2015\)](#) for non-rotating convection (b) Viscous boundary layer thickness at the inner boundary (λ_U^i) normalised by $Re_c^{-1/2}$ as a function of $RaE^{12/7}$. The dotted vertical lines correspond to the Rayleigh number $Ra = 100 E^{-12/7}$ beyond which λ_T^i and λ_U^i adopt scaling behaviours close to the non-rotating RBC. The symbols have the same meaning as in figure 1.

container L . In spherical shells however, the absence of sidewalls precludes the formation of such a global and single cell LSC structure. The typical flow length scale can instead be estimated by the average inter-plume distance ([King et al. 2013](#)). In our previous study ([Gastine et al. 2015](#)), we established the following scaling for the plume spacing

$$\ell_{NR}/L \sim Ra^{1/2} Nu^{-5/2}. \quad (3.27)$$

Figure 18(b) shows the calculations of ℓ renormalised by ℓ_{NR} versus the transition parameter $RaE^{12/7}$. Though the collapse of the data, especially when $RaE^{12/7} < 1$, is not as good as those obtained for Nu , $\tilde{\epsilon}_U$ and Re_c , the transition parameter (3.26) provides an effective way to capture the transition of the mean flow length scale from rotating (equation 3.20) to non-rotating (equation 3.27) convection. For $RaE^{12/7} > 100$ (dotted vertical line), ℓ approaches the non-rotating scaling ℓ_{NR} (3.27).

3.3.3. Thermal and viscous boundary layers

In figure 19 we examine calculations of the thermal and viscous boundary layer thicknesses at the inner boundary renormalised by their asymptotic scalings in non-rotating convection plotted versus $RaE^{12/7}$. Once again, the renormalisation of the axes allows us to collapse the boundary layer thicknesses for all E on one single curve. The transition parameter $RaE^{12/7}$ therefore provides an accurate way of distinguishing the variations of most of the physical quantities considered in this study across the regime change from rotating to non-rotating convection.

Beyond $RaE^{12/7} = \mathcal{O}(10^2)$, all the diagnostic quantities for the rotating models becomes statistically indiscernible from the non-rotating behaviour. This value can therefore be adopted to define the upper bound of the transitional regime.

4. Conclusion and outlooks

We have studied rotating convection in spherical shells by means of three-dimensional direct numerical simulations. We have constructed a dataset of more than 200 models that cover a broad parameter range with Ekman numbers spanning $3 \times 10^{-7} \leq E \leq 10^{-1}$,

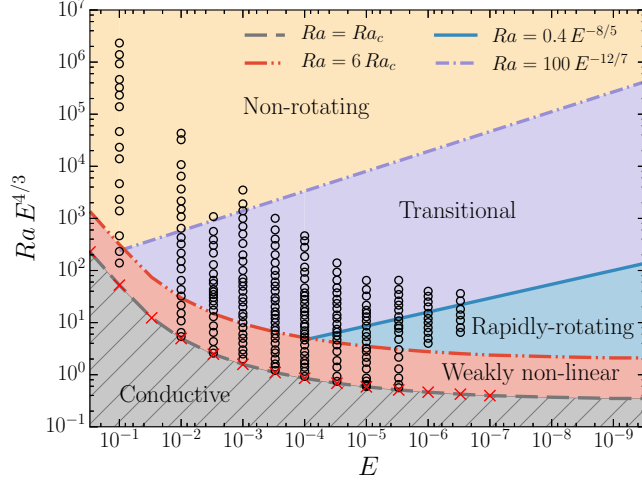


FIGURE 20. Regime diagram that summarises the regime transitions. The black circles correspond to the numerical simulations carried out in this study, while the red crosses mark the critical Rayleigh numbers Ra_c given in table B1.

Rayleigh numbers within the range $10^3 < Ra < 2 \times 10^{10}$. The Prandtl number Pr is one and the radius ratio r_i/r_o is 0.6 in all cases. Figure 20 shows the parameter space covered by our numerical dataset as well as the regime boundaries of rotating convection derived in this work. We have studied seven different diagnostic quantities and investigated their scaling properties across the regime changes from onset of rotating convection to weakly-rotating convection. These quantities encompass the Nusselt number Nu , the Reynolds number Re_c , the dimensionless viscous dissipation rate $\tilde{\epsilon}_U$, the interior temperature gradient β_T , the average flow length scale ℓ and the thermal and viscous boundary layer thicknesses λ_T and λ_U . The scaling behaviours of these seven quantities of interest are summarised in table 1.

For Ra just above critical (i.e. $Ra \gtrsim Ra_c$), our numerical simulations have confirmed the scaling relation of the form $Nu - 1 \sim Ra/Ra_c - 1$, predicted by the perturbation analysis by Busse & Or (1986) and Gillet & Jones (2006). In this weakly non-linear regime of rotating convection, the convective flow is laminar and takes the form of a drifting thermal Rossby wave with a typical size of $\ell/L \sim E^{1/3}$. The triple force balance between viscosity, Coriolis force and buoyancy (the so-called VAC balance), suggests the scaling for the flow velocity $Re_c \sim Ra_Q^{1/2} E^{1/3}$, which is in good agreement with the numerical data.

In the limit of small Ekman numbers, an increase of the supercriticality is accompanied by a gradual transition to a turbulent quasi-geostrophic regime (when $Ra \geq 6 Ra_c$ and $Nu > 2$). The heat transport scaling is then expected to become independent of the thermal and viscous diffusivities and to depend only on the supercriticality Ra/Ra_c , yielding $Nu \sim Ra^{3/2} E^2$ (see Gillet & Jones 2006; Julien *et al.* 2012b; Stellmach *et al.* 2014). A small subset of our numerical data has been found to approach this asymptotic scaling in a narrow fraction of the parameter space delimited by $6 Ra_c \leq Ra \leq 0.4 E^{-8/5}$. In good agreement with the theory by Julien *et al.* (2012b), we have observed a breakdown of the $Ra^{3/2}$ scaling law when the thermal boundary layer is not dominated by rotational effects any longer, i.e. when $Ra E^{8/5} = \mathcal{O}(1)$.

Thanks to a decomposition of the dimensionless viscous dissipation rate $\tilde{\epsilon}_U$ into bulk and boundary layer contributions, we derived a theoretical scaling of the form $\tilde{\epsilon}_U E^{1/2} \sim$

Regime	Weakly non-linear $Ra_c < Ra < 6 Ra_c$ VAC		Rapidly-rotating $6 Ra_c < Ra < 0.4 E^{-8/5}$ bulk CIA+Ekman friction		Non-rotating $Ra > 100 E^{-12/7}$ IA	
	Scaling	Reference	Scaling	Reference	Scaling	Reference
Nu	$a \left(\frac{Ra}{Ra_c} - 1 \right) + 1$	Equation (3.2) Figure 3(a)	$\frac{Ra^{3/2} E^2}{Pr^{1/2}}$	Equation (1.1) Figures 5-6	$Ra^{0.27}$ to $Ra^{1/3}$	Figures 1 and 16
$\tilde{\epsilon}_U$	$\frac{Re_c^2}{E^{2/3}}$	Equation (3.3)	$a \frac{Re_c^2}{E^{1/2}} + b \frac{Re_c^{5/2}}{E^{1/2}}$	Equation (3.15) Figure 8	$a Re_c^{5/2} + b Re_c^3$	Figure 17(a)
Re_c	$\left(\frac{Ra_Q E^{2/3}}{Pr^2} \right)^{1/2}$	Equation (3.5) Figure 3(b)	$\left(\frac{Ra_Q E^{1/2}}{Pr^2} \right)^{1/2}$ to $\left(\frac{Ra_Q E^{1/2}}{Pr^2} \right)^{2/5}$	Equation (3.16) Figure 9	$Ra^{0.46}$ to $Ra^{1/2}$	Figure 17(b)
$-\beta_T$	$\frac{4\eta}{(1+\eta)^2}$	Equation (2.7)	$\frac{Nu}{Re_c^{3/2} E^{1/2}}?$	Equation (3.21) Figure 12	0	Figures 12 and 18(a)
ℓ/L	$E^{1/3}$	Equation (3.4) Figure 4	$Re_c^{1/2} E^{1/2}$	Equation (3.20) Figure 10	$\frac{Ra^{1/2}}{Nu^{5/2}}$	Equation (3.27) Figure 18(b)
λ_T/L	Undefined		$0.2 Nu^{-1+o(E)}?$	Equation (3.23) Figure 13	$0.5 Nu^{-1}$	Equation (3.23) Figures 13 and 19(a)
λ_U/L	$E^{1/2}$	Equation (3.25) Figure 14	$E^{1/2}$	Equation (3.25) Figure 14	$Re^{-1/2}$	Equation (3.24) Figures 14 and 19(b)

Scaling regimes in spherical shell rotating convection

TABLE 1. Summary table of the scaling properties of the quantities of interest in the different regimes of rotating convection derived in this work. The acronyms employed on the third line stand for the leading-order force balance: *Visco-Archimedean-Coriolis* (VAC), *Coriolis-Inertia-Archimedean* (CIA) and *Inertia-Archimedean* (IA). The notation $o(E)$ designates a weak-dependence on the Ekman number, while the question marks highlight possible uncertainties on the scaling laws. See text for the successive derivation of scalings.

$(a Re^{5/2} + b Re^2)$, which accurately describes the numerical data when adjusting the two fit parameters a and b . A sizeable fraction of the dissipation occurs in the fluid bulk, which is dominated by a triple force balance between Coriolis, Inertia and buoyancy (the so-called inertial theory of rotating convection or CIA balance, e.g. [Aubert et al. 2001](#)). The remaining fraction of the dissipation can be attributed to the viscous friction in the Ekman boundary layers. In contrast to the existing scalings that neglect the boundary layer dissipation ([Aubert et al. 2001](#); [Gillet & Jones 2006](#); [King & Buffett 2013](#); [Barker et al. 2014](#)), this scaling law accurately captures the scaling behaviour of the Reynolds number. Our scaling further predicts that the bulk dissipation will dominate when $Re_c > 5000$. Beyond this value, the inertial scaling for rotating convection $Re_c \sim Ra_Q^{2/5} E^{1/5}$ and $\ell \sim \sqrt{Re_c E} L$ (Rhines scaling) should be gradually approached.

Beyond $Ra = 0.4 E^{-8/5}$, the rotational constraint on the convective flow gradually decreases until the dynamics resembles non-rotating convection. Within this parameter range, that we designate as the *transitional regime*, we have observed continuous changes of the flow properties. The heat transfer scaling exponents show continuous variations that depend on Ra and E rather than simple polynomial laws. This makes the derivation of asymptotic scalings inherent to this physical regime extremely difficult. From the intersection between the steep $Nu \sim Ra^{3/2} E^2$ scaling for rapidly-rotating convection and the shallow exponent for non-rotating convection $Nu \sim Ra^{1/3}$, we have defined a transition Rayleigh number $Ra_T \sim E^{-12/7}$, which indeed allows to separate the rotation-influenced solutions from those resembling non-rotating convection. Beyond $Ra E^{12/7} \sim \mathcal{O}(10^2)$, all the diagnostic quantities studied here follow the scalings for non-rotating convection ([Gastine et al. 2015](#)). This defines the upper bound of the transitional regime displayed in the regime diagram (figure 20).

Our systematic study of rotating convection in spherical shells revealed interesting differences to the local simulations carried out in cartesian coordinates ([King et al. 2012](#); [Stellmach et al. 2014](#); [Cheng et al. 2015](#)). In the limit of small Ekman numbers ($E = \mathcal{O}(10^{-7})$), these studies have obtained much steeper heat transfer scaling laws (from $Nu \sim Ra^3 E^4$ to $Nu \sim Ra^{3.6} E^{4.8}$) than our findings. This has been attributed to an active role of the Ekman boundary layers, which supposedly promotes very efficient heat transfer, much steeper than the diffusivity-free asymptotic scaling ([Julien et al. 2016](#)). In spherical geometry, the Ekman pumping might play a significant role and may indeed affect the heat transport in the polar regions where gravity is aligned with the rotation axis. As shown by [Yadav et al. \(2016\)](#), the heat transport in spherical shells with rigid mechanical boundaries is however dominated by the equatorial regions, where the influence of Ekman pumping on the heat transfer might be negligible. A regional analysis of the heat transport in spherical shell models as well as the computation of new cartesian models in which gravity is orthogonal to the rotation axis could possibly help to ascertain this scenario.

Dynamo processes and convection in planetary and stellar interiors frequently operate at Prandtl numbers much smaller than unity. The parameter study presented here has been focused on the peculiar case of $Pr = 1$. It would be interesting to complement our study with simulations with $Pr = \mathcal{O}(10^{-2} - 10^{-1})$ to verify the theoretical Pr -scalings derived here (see table 1). Recent studies by [King & Aurnou \(2013\)](#) and [Guervilly & Cardin \(2016\)](#) indeed reveal interesting new physical phenomena inherent to small Prandtl number fluids that could possibly impact the scaling properties.

The authors wish to thank Jonathan Aurnou and Keith Julien for fruitful scientific discussions and constructive criticisms at different stages of this research work. All the computations have been carried out on the GWDG computer facilities in Göttingen, on the IBM iDataPlex HPC System Hydra at the MPG Rechenzentrum Garching and on

the S-CAPAD platform at IPGP. TG has been partly supported by the Special Priority Program 1488 (PlanetMag, www.planetmag.de) of the German Science Foundation. This is IPGP contribution 3780.

Appendix A. Table of results

#	Ra	Nu	Re_c	β_T	ℓ	λ_T^i/L	λ_U^i/L	χ_T	χ_U	$N_r \times \ell_{max}$
$E = 10^{-1}$										
1	3×10^3	1.71	0.0	-0.18	0.704	—	—	1.000	1.000	61×64
2	5×10^3	2.04	12.7	-0.07	0.665	—	—	1.002	1.003	61×133
3	1×10^4	2.47	21.6	0.03	0.638	—	—	1.000	1.000	61×133
4	3×10^4	3.39	42.6	0.02	0.481	1.2×10^{-1}	5.5×10^{-2}	1.001	1.002	61×133
5	5×10^4	3.88	55.1	0.01	0.420	1.0×10^{-1}	4.9×10^{-2}	1.000	1.000	61×133
6	1×10^5	4.71	79.1	0.00	0.361	8.5×10^{-2}	4.3×10^{-2}	1.002	1.003	61×133
7	3×10^5	6.38	137.8	0.00	0.298	6.3×10^{-2}	3.3×10^{-2}	1.001	1.001	61×133
8	5×10^5	7.37	176.8	0.00	0.270	5.4×10^{-2}	3.0×10^{-2}	1.000	1.000	61×133
9	1×10^6	8.90	250.5	-0.01	0.239	4.5×10^{-2}	2.6×10^{-2}	1.000	1.000	81×170
10	3×10^6	12.08	426.2	-0.01	0.206	3.3×10^{-2}	2.0×10^{-2}	1.000	1.000	97×213
11	5×10^6	13.97	539.5	-0.01	0.192	2.8×10^{-2}	1.8×10^{-2}	1.000	1.001	97×256
12	7×10^6	15.45	646.7	-0.01	0.184	2.5×10^{-2}	1.7×10^{-2}	1.000	1.003	97×213
13	1×10^7	17.12	763.0	-0.01	0.174	2.3×10^{-2}	1.6×10^{-2}	1.001	1.006	97×266
14	2×10^7	20.85	1045.5	-0.01	0.161	1.9×10^{-2}	1.3×10^{-2}	1.000	1.005	129×426
15	3×10^7	23.44	1288.5	-0.01	0.155	1.7×10^{-2}	1.2×10^{-2}	1.000	1.007	129×426
16	5×10^7	27.41	1611.5	-0.03	0.144	1.4×10^{-2}	1.1×10^{-2}	1.001	1.025	129×426
$E = 10^{-2}$										
17	2.5×10^3	1.062	2.3	-0.87	0.404	—	—	1.000	1.000	61×85
18	3×10^3	1.19	4.5	-0.74	0.400	—	—	1.000	1.000	61×85
19	5×10^3	1.47	8.0	-0.54	0.298	—	—	1.000	1.000	61×85
20	7×10^3	1.69	12.1	-0.40	0.376	—	—	1.000	1.000	61×85
21	1×10^4	2.03	17.1	-0.25	0.366	—	—	0.999	0.998	61×85
22	1.5×10^4	2.38	23.4	-0.16	0.362	—	—	1.000	1.001	61×85
23	2×10^4	2.64	28.6	-0.13	0.362	—	—	0.999	0.999	61×85
24	3×10^4	3.05	37.1	-0.09	0.353	1.2×10^{-1}	5.1×10^{-2}	1.001	1.001	61×85
25	5×10^4	3.66	51.1	-0.06	0.348	1.1×10^{-1}	4.8×10^{-2}	1.000	1.000	61×85
26	7×10^4	4.09	62.3	-0.04	0.342	9.5×10^{-2}	4.5×10^{-2}	1.000	1.001	61×85
27	1×10^5	4.59	76.5	-0.03	0.331	8.6×10^{-2}	4.3×10^{-2}	0.998	0.997	61×133
28	1.5×10^5	5.18	95.7	-0.02	0.319	7.7×10^{-2}	3.8×10^{-2}	1.000	1.000	61×133
29	2×10^5	5.61	111.0	-0.01	0.310	7.1×10^{-2}	3.6×10^{-2}	0.999	0.998	61×133
30	3×10^5	6.36	137.9	-0.00	0.291	6.3×10^{-2}	3.3×10^{-2}	1.001	1.001	49×85
31	5×10^5	7.33	178.5	-0.00	0.270	5.4×10^{-2}	3.0×10^{-2}	1.000	1.000	61×133
32	7×10^5	8.05	210.4	-0.00	0.257	4.9×10^{-2}	2.8×10^{-2}	1.000	1.000	61×133
33	1×10^6	8.90	246.8	-0.01	0.242	4.5×10^{-2}	2.6×10^{-2}	1.000	1.000	61×133
34	1.7×10^6	10.30	319.4	-0.01	0.226	3.8×10^{-2}	2.3×10^{-2}	1.000	1.000	97×256
35	3×10^6	12.08	423.8	-0.01	0.202	3.3×10^{-2}	2.0×10^{-2}	1.000	1.000	97×256
36	5×10^6	13.98	537.5	-0.01	0.191	2.8×10^{-2}	1.8×10^{-2}	1.000	1.001	97×256
37	1.5×10^7	19.25	922.2	-0.01	0.168	2.1×10^{-2}	1.5×10^{-2}	0.998	1.017	97×341

38	2×10^7	20.82	1074.3	-0.00	0.166	1.9×10^{-2}	1.3×10^{-2}	0.999	1.006	121×426
----	-----------------	-------	--------	-------	-------	----------------------	----------------------	-------	-------	------------------

$E = 3 \times 10^{-3}$

39	6×10^3	1.022	1.9	-0.92	0.380	—	—	1.000	1.000	61×85
40	7×10^3	1.097	4.3	-0.87	0.376	—	—	1.000	1.000	61×85
41	1×10^4	1.26	8.2	-0.77	0.365	—	—	1.000	1.000	61×85
42	1.5×10^4	1.52	11.9	-0.59	0.238	—	—	1.000	1.000	61×85
43	2×10^4	1.70	15.9	-0.54	0.254	—	—	1.003	1.007	61×85
44	3×10^4	2.12	23.9	-0.40	0.260	—	—	1.000	1.000	61×85
45	4×10^4	2.54	31.5	-0.29	0.261	—	—	1.000	1.000	61×85
46	5×10^4	2.86	38.2	-0.24	0.263	—	—	1.000	1.000	61×85
47	6×10^4	3.13	44.2	-0.20	0.265	1.0×10^{-1}	3.8×10^{-2}	1.000	1.000	61×85
48	7×10^4	3.35	49.7	-0.18	0.267	9.9×10^{-2}	3.8×10^{-2}	1.000	1.000	61×85
49	8×10^4	3.55	54.9	-0.17	0.269	9.5×10^{-2}	3.7×10^{-2}	0.999	0.999	61×106
50	9×10^4	3.72	59.6	-0.16	0.269	9.1×10^{-2}	3.7×10^{-2}	0.999	0.998	61×106
51	1×10^5	3.87	64.0	-0.15	0.270	8.8×10^{-2}	3.6×10^{-2}	1.000	1.000	73×106
52	1.3×10^5	4.28	76.1	-0.13	0.267	8.0×10^{-2}	3.5×10^{-2}	1.000	1.000	73×106
53	1.5×10^5	4.50	83.2	-0.12	0.265	7.7×10^{-2}	3.4×10^{-2}	1.000	1.000	73×106
54	2×10^5	4.99	98.7	-0.11	0.259	7.0×10^{-2}	3.3×10^{-2}	1.000	1.000	73×106
55	3×10^5	5.76	123.8	-0.10	0.250	6.2×10^{-2}	3.0×10^{-2}	1.000	1.000	81×128
56	5×10^5	6.88	159.8	-0.08	0.239	5.3×10^{-2}	2.8×10^{-2}	1.000	1.000	81×133
57	7×10^5	7.70	190.0	-0.06	0.234	4.8×10^{-2}	2.7×10^{-2}	0.999	0.999	81×133
58	9×10^5	8.36	217.0	-0.05	0.230	4.5×10^{-2}	2.5×10^{-2}	1.000	0.999	97×170
59	1.3×10^6	9.37	266.6	-0.04	0.222	4.1×10^{-2}	2.3×10^{-2}	1.000	1.000	97×170
60	2.5×10^6	11.39	380.8	-0.02	0.207	3.4×10^{-2}	2.0×10^{-2}	1.000	1.000	97×213

$E = 10^{-3}$

61	2×10^4	1.076	4.8	-0.90	0.224	—	—	1.000	1.000	65×85
62	2.5×10^4	1.16	7.5	-0.86	0.223	—	—	1.000	1.000	65×85
63	3×10^4	1.20	8.5	-0.85	0.194	—	—	1.000	1.000	65×85
64	4×10^4	1.28	11.0	-0.83	0.177	—	—	1.000	1.000	65×85
65	5×10^4	1.44	15.4	-0.74	0.186	—	—	1.000	1.000	65×85
66	6×10^4	1.60	19.1	-0.64	0.177	—	—	1.000	1.000	65×85
67	8×10^4	1.87	26.4	-0.59	0.190	—	—	1.001	1.003	65×85
68	1×10^5	2.24	34.5	-0.52	0.191	—	—	1.000	0.999	65×85
69	1.3×10^5	2.77	45.7	-0.43	0.190	—	—	0.999	0.999	65×85
70	1.5×10^5	3.08	52.3	-0.38	0.190	8.5×10^{-2}	2.7×10^{-2}	1.000	1.001	65×85
71	2×10^5	3.73	67.3	-0.32	0.190	7.5×10^{-2}	2.6×10^{-2}	1.000	0.999	65×85
72	2.5×10^5	4.22	80.0	-0.28	0.191	6.9×10^{-2}	2.6×10^{-2}	1.000	1.000	65×85
73	3×10^5	4.64	91.6	-0.26	0.191	6.4×10^{-2}	2.5×10^{-2}	1.000	1.000	65×85
74	4×10^5	5.44	115.4	-0.20	0.193	5.8×10^{-2}	2.5×10^{-2}	1.000	0.999	65×85
75	5×10^5	5.97	133.7	-0.19	0.192	5.4×10^{-2}	2.4×10^{-2}	1.000	0.999	65×85
76	6×10^5	6.42	150.6	-0.18	0.191	5.0×10^{-2}	2.3×10^{-2}	1.000	0.999	65×85
77	7×10^5	6.77	165.9	-0.17	0.190	4.8×10^{-2}	2.3×10^{-2}	1.000	1.000	81×106
78	1×10^6	7.68	206.7	-0.15	0.190	4.3×10^{-2}	2.1×10^{-2}	1.000	1.000	81×133
79	1.5×10^6	8.91	264.2	-0.13	0.187	3.8×10^{-2}	2.0×10^{-2}	1.001	1.001	81×133
80	2×10^6	9.86	310.7	-0.12	0.184	3.4×10^{-2}	1.9×10^{-2}	1.000	1.000	81×133
81	3.3×10^6	11.84	405.1	-0.10	0.180	2.9×10^{-2}	1.8×10^{-2}	1.000	1.001	81×133
82	5×10^6	13.38	476.1	-0.09	0.170	2.7×10^{-2}	1.7×10^{-2}	1.000	1.001	97×213
83	7×10^6	14.95	556.7	-0.07	0.167	2.4×10^{-2}	1.6×10^{-2}	1.000	1.003	97×213

84	1×10^7	16.91	673.2	-0.05	0.163	2.2×10^{-2}	1.5×10^{-2}	1.000	1.007	97×213
85	1.4×10^7	18.60	807.9	-0.05	0.160	2.0×10^{-2}	1.3×10^{-2}	0.999	1.007	97×266
86	1.9×10^7	20.49	966.2	-0.03	0.153	1.9×10^{-2}	1.2×10^{-2}	1.000	1.006	121×341
87	3.5×10^7	24.52	1231.8	-0.02	0.146	1.6×10^{-2}	1.1×10^{-2}	0.999	1.011	129×426

 $E = 3 \times 10^{-4}$

88	6×10^4	1.022	3.4	-0.94	0.173	—	—	1.000	1.000	65×106
89	7×10^4	1.060	6.0	-0.94	0.173	—	—	1.000	1.000	65×106
90	8×10^4	1.090	7.8	-0.93	0.174	—	—	1.000	1.000	65×106
91	1×10^5	1.14	10.3	-0.92	0.173	—	—	1.000	1.000	65×106
92	1.3×10^5	1.18	13.2	-0.93	0.171	—	—	1.000	1.000	65×106
93	1.5×10^5	1.22	15.3	-0.92	0.171	—	—	1.000	1.000	65×106
94	2×10^5	1.39	21.2	-0.82	0.140	—	—	1.000	1.000	65×106
95	2.5×10^5	1.53	27.1	-0.76	0.136	—	—	1.000	1.000	65×106
96	3×10^5	1.75	34.9	-0.70	0.135	—	—	1.000	1.000	65×106
97	3.5×10^5	2.04	43.7	-0.64	0.136	—	—	1.000	1.000	65×106
98	4×10^5	2.33	52.2	-0.59	0.136	—	—	1.000	1.000	65×106
99	5×10^5	2.91	68.4	-0.51	0.138	—	—	1.000	1.001	73×128
100	6×10^5	3.49	83.6	-0.45	0.139	6.5×10^{-2}	1.8×10^{-2}	1.000	1.000	73×128
101	7×10^5	4.03	97.9	-0.40	0.140	5.9×10^{-2}	1.7×10^{-2}	1.000	1.000	73×128
102	8×10^5	4.51	111.2	-0.36	0.140	5.5×10^{-2}	1.7×10^{-2}	1.000	1.000	73×128
103	1×10^6	5.36	135.4	-0.31	0.142	4.9×10^{-2}	1.7×10^{-2}	1.001	1.001	73×128
104	1.3×10^6	6.38	167.0	-0.27	0.142	4.4×10^{-2}	1.6×10^{-2}	0.999	0.999	73×128
105	1.5×10^6	6.92	185.5	-0.26	0.144	4.1×10^{-2}	1.6×10^{-2}	1.000	1.000	73×128
106	2×10^6	8.04	227.9	-0.23	0.144	3.7×10^{-2}	1.5×10^{-2}	1.000	0.999	73×128
107	2.5×10^6	8.89	264.3	-0.22	0.144	3.4×10^{-2}	1.5×10^{-2}	0.999	0.998	73×128
108	3×10^6	9.63	298.4	-0.21	0.144	3.1×10^{-2}	1.5×10^{-2}	1.000	0.999	81×133
109	4×10^6	10.87	358.2	-0.20	0.143	2.8×10^{-2}	1.4×10^{-2}	1.000	0.999	81×133
110	5×10^6	11.97	412.1	-0.20	0.140	2.6×10^{-2}	1.4×10^{-2}	1.001	0.999	81×133
111	7×10^6	13.42	501.0	-0.18	0.136	2.4×10^{-2}	1.3×10^{-2}	1.000	1.000	97×170
112	1×10^7	15.16	614.0	-0.16	0.132	2.1×10^{-2}	1.2×10^{-2}	1.000	1.003	97×256
113	1.5×10^7	17.49	779.4	-0.13	0.133	1.9×10^{-2}	1.1×10^{-2}	1.001	1.004	97×341
114	2×10^7	19.40	908.0	-0.13	0.133	1.7×10^{-2}	1.1×10^{-2}	1.001	1.010	97×341
115	3×10^7	22.33	1076.3	-0.10	0.121	1.6×10^{-2}	1.0×10^{-2}	1.000	1.009	121×426
116	5×10^7	26.15	1377.0	-0.09	0.123	1.4×10^{-2}	9.4×10^{-3}	1.001	1.010	161×512

 $E = 10^{-4}$

117	2×10^5	1.014	3.9	-0.94	0.133	—	—	1.000	1.000	73×85
118	2.5×10^5	1.052	8.1	-0.96	0.134	—	—	1.000	1.000	73×85
119	3×10^5	1.081	10.7	-0.96	0.134	—	—	1.000	1.000	73×85
120	3.5×10^5	1.10	12.7	-0.96	0.134	—	—	1.000	1.000	73×85
121	4×10^5	1.12	14.4	-0.96	0.133	—	—	1.000	1.000	73×85
122	5×10^5	1.18	19.5	-0.92	0.131	—	—	1.000	1.000	73×85
123	6×10^5	1.25	24.4	-0.87	0.124	—	—	1.000	1.000	73×85
124	8×10^5	1.32	30.7	-0.86	0.124	—	—	1.000	1.000	73×85
125	1×10^6	1.50	40.3	-0.79	0.113	—	—	1.001	1.002	73×85
126	1.15×10^6	1.69	49.5	-0.74	0.109	—	—	1.002	1.005	73×85
127	1.3×10^6	1.95	60.5	-0.69	0.107	—	—	1.000	1.002	73×85
128	1.5×10^6	2.29	74.7	-0.65	0.108	—	—	1.000	1.000	81×128
129	1.8×10^6	2.87	95.8	-0.60	0.107	—	—	1.000	0.999	73×85

130	2×10^6	3.19	109.1	-0.55	0.108	6.1×10^{-2}	1.2×10^{-2}	1.000	1.000	81×128
131	2.5×10^6	4.10	141.4	-0.48	0.110	5.0×10^{-2}	1.1×10^{-2}	1.000	1.000	81×128
132	3×10^6	4.99	172.0	-0.43	0.114	4.3×10^{-2}	1.1×10^{-2}	1.000	1.000	81×128
133	3.5×10^6	5.82	200.4	-0.39	0.115	3.9×10^{-2}	1.1×10^{-2}	1.000	0.999	81×128
134	4×10^6	6.58	226.5	-0.36	0.116	3.5×10^{-2}	1.0×10^{-2}	1.000	0.999	81×128
135	5×10^6	7.92	274.7	-0.33	0.117	3.1×10^{-2}	1.0×10^{-2}	1.000	0.999	81×128
136	6×10^6	9.01	317.7	-0.31	0.118	2.8×10^{-2}	10.0×10^{-3}	1.000	0.998	81×128
137	7×10^6	9.90	355.9	-0.30	0.118	2.6×10^{-2}	9.8×10^{-3}	1.000	0.998	81×128
138	8×10^6	10.68	391.8	-0.29	0.119	2.5×10^{-2}	9.8×10^{-3}	1.000	0.998	81×133
139	1×10^7	12.02	457.9	-0.26	0.119	2.3×10^{-2}	9.6×10^{-3}	1.000	1.000	81×170
140	1.5×10^7	14.41	590.3	-0.24	0.119	2.0×10^{-2}	9.6×10^{-3}	1.000	1.001	97×213
141	2×10^7	16.38	707.5	-0.23	0.119	1.8×10^{-2}	9.3×10^{-3}	1.000	1.003	97×213
142	2.5×10^7	18.16	816.2	-0.22	0.118	1.6×10^{-2}	8.9×10^{-3}	1.001	1.008	97×213
143	4×10^7	21.54	1094.5	-0.19	0.111	1.4×10^{-2}	8.0×10^{-3}	1.000	1.006	121×341
144	6×10^7	25.18	1371.3	-0.17	0.104	1.3×10^{-2}	7.4×10^{-3}	1.000	1.010	161×426
145	8×10^7	28.02	1583.3	-0.16	0.100	1.1×10^{-2}	7.0×10^{-3}	0.999	1.003	201×512
146	1×10^8	30.75	1785.6	-0.14	0.097	1.1×10^{-2}	6.8×10^{-3}	1.001	1.011	201×682

 $E = 3 \times 10^{-5}$

147	8×10^5	1.010	4.7	-0.94	0.089	—	—	1.000	1.000	65×128
148	1×10^6	1.036	9.6	-0.96	0.093	—	—	1.000	1.000	65×128
149	1.5×10^6	1.086	17.0	-0.97	0.091	—	—	1.000	1.000	65×128
150	2×10^6	1.15	25.9	-0.95	0.091	—	—	1.000	1.000	65×128
151	3×10^6	1.25	40.2	-0.91	0.096	—	—	1.000	1.000	65×128
152	4×10^6	1.38	54.3	-0.85	0.086	—	—	1.000	1.000	65×128
153	5×10^6	1.60	71.1	-0.78	0.077	—	—	1.000	1.000	65×133
154	6×10^6	1.96	94.8	-0.71	0.075	—	—	1.000	1.000	65×133
155	7×10^6	2.39	121.0	-0.67	0.076	—	—	1.000	0.999	65×133
156	8×10^6	2.80	146.2	-0.63	0.078	—	—	1.000	1.000	65×170
157	1×10^7	3.72	197.0	-0.56	0.082	5.0×10^{-2}	7.0×10^{-3}	1.000	1.000	97×170
158	1.3×10^7	5.12	270.5	-0.48	0.085	3.8×10^{-2}	6.5×10^{-3}	1.001	1.001	65×170
159	1.5×10^7	6.04	315.7	-0.45	0.087	3.2×10^{-2}	6.3×10^{-3}	1.001	1.001	65×170
160	2×10^7	8.30	423.0	-0.38	0.090	2.6×10^{-2}	6.2×10^{-3}	1.000	1.000	97×213
161	2.5×10^7	10.31	514.9	-0.34	0.091	2.2×10^{-2}	6.1×10^{-3}	1.000	1.001	97×256
162	3×10^7	11.95	596.9	-0.32	0.092	2.0×10^{-2}	6.0×10^{-3}	1.000	1.001	97×256
163	4×10^7	14.65	745.2	-0.29	0.093	1.7×10^{-2}	5.9×10^{-3}	1.001	1.002	97×341
164	5×10^7	16.58	864.1	-0.28	0.094	1.5×10^{-2}	5.8×10^{-3}	1.003	1.005	97×341
165	7×10^7	19.71	1086.3	-0.26	0.094	1.4×10^{-2}	5.7×10^{-3}	1.002	1.004	129×426
166	1×10^8	23.34	1350.8	-0.25	0.095	1.2×10^{-2}	5.6×10^{-3}	1.003	1.007	129×512
167	1.5×10^8	27.96	1722.8	-0.23	0.096	1.0×10^{-2}	5.2×10^{-3}	1.004	1.012	161×682

 $E = 10^{-5}$

168	2.75×10^6	1.001	1.9	-0.94	0.061	—	—	1.000	0.999	97×133
169	2.85×10^6	1.004	4.2	-0.94	0.061	—	—	1.000	0.999	97×133
170	2.9×10^6	1.006	4.9	-0.94	0.061	—	—	1.000	0.999	97×133
171	2.95×10^6	1.008	5.6	-0.94	0.061	—	—	1.000	1.000	97×133
172	3×10^6	1.009	6.2	-0.94	0.061	—	—	1.000	1.000	97×133
173	3.5×10^6	1.023	10.3	-0.95	0.061	—	—	1.000	1.000	97×133
174	4×10^6	1.035	13.0	-0.96	0.061	—	—	1.000	0.999	97×170
175	6×10^6	1.089	25.4	-0.99	0.063	—	—	1.000	1.000	97×170

176	8×10^6	1.15	37.4	-0.99	0.066	—	—	1.000	1.000	97×170
177	1×10^7	1.19	47.9	-0.95	0.066	—	—	1.000	1.001	97×170
178	1.3×10^7	1.28	65.6	-0.90	0.066	—	—	1.000	1.002	97×170
179	1.5×10^7	1.33	75.6	-0.87	0.064	—	—	1.000	1.000	97×170
180	2×10^7	1.61	106.5	-0.80	0.056	—	—	1.000	0.998	97×170
181	2.5×10^7	1.94	141.8	-0.74	0.055	—	—	1.000	0.999	97×213
182	3×10^7	2.47	190.5	-0.69	0.057	—	—	1.000	1.000	97×213
183	4×10^7	3.64	291.0	-0.61	0.061	4.8×10^{-2}	4.6×10^{-3}	1.000	1.000	97×213
184	5×10^7	4.90	390.4	-0.54	0.065	3.6×10^{-2}	4.4×10^{-3}	1.000	1.001	97×213
185	6×10^7	6.17	486.3	-0.49	0.067	2.9×10^{-2}	4.2×10^{-3}	1.002	1.002	97×213
186	7×10^7	7.45	576.1	-0.45	0.069	2.6×10^{-2}	4.1×10^{-3}	1.002	1.005	97×213
187	8×10^7	8.88	675.7	-0.41	0.073	2.2×10^{-2}	4.1×10^{-3}	1.003	1.004	97×341
188	1×10^8	11.40	838.6	-0.37	0.074	1.8×10^{-2}	4.0×10^{-3}	1.006	1.006	97×341
189	1.5×10^8	16.21	1171.5	-0.33	0.076	1.4×10^{-2}	3.6×10^{-3}	1.002	1.007	129×341
190	2×10^8	20.07	1457.3	-0.31	0.078	1.2×10^{-2}	3.6×10^{-3}	1.006	1.011	129×426
191	3×10^8	25.66	1903.0	-0.29	0.081	9.6×10^{-3}	3.5×10^{-3}	1.006	1.015	161×682

 $E = 3 \times 10^{-6}$

192	1.3×10^7	1.007	7.6	-0.94	0.040	—	—	1.000	0.999	97×192
193	1.5×10^7	1.015	12.2	-0.95	0.043	—	—	1.000	0.997	97×192
194	2×10^7	1.043	22.6	-0.97	0.041	—	—	1.000	0.999	97×192
195	3×10^7	1.10	41.5	-0.99	0.041	—	—	1.000	1.000	97×266
196	5×10^7	1.21	81.0	-0.95	0.044	—	—	1.000	1.001	129×341
197	7×10^7	1.32	115.2	-0.88	0.044	—	—	1.000	1.000	129×341
198	1.1×10^8	1.71	188.7	-0.78	0.040	—	—	1.000	1.000	129×426
199	1.5×10^8	2.52	311.5	-0.70	0.042	—	—	0.999	1.004	129×341
200	1.8×10^8	3.26	415.9	-0.65	0.045	5.3×10^{-2}	2.7×10^{-3}	1.002	1.003	129×341
201	2×10^8	3.80	493.1	-0.62	0.047	4.6×10^{-2}	2.7×10^{-3}	1.003	1.003	129×426
202	2.5×10^8	5.30	678.2	-0.56	0.051	3.4×10^{-2}	2.5×10^{-3}	1.001	1.003	129×512
203	3×10^8	6.78	854.4	-0.50	0.054	2.6×10^{-2}	2.4×10^{-3}	1.005	1.003	129×426
204	4×10^8	9.87	1190.1	-0.43	0.057	1.9×10^{-2}	2.3×10^{-3}	1.011	1.009	129×512
205	5×10^8	12.96	1504.7	-0.39	0.059	1.4×10^{-2}	2.2×10^{-3}	1.004	1.009	161×512
206	6×10^8	16.10	1794.0	-0.36	0.060	1.2×10^{-2}	2.2×10^{-3}	1.015	1.009	$201 \times 682^*$
207	8×10^8	20.99	2209.9	-0.34	0.063	9.5×10^{-3}	2.1×10^{-3}	1.004	1.013	$201 \times 682^{***}$
208	1×10^9	25.17	2622.5	-0.32	0.064	8.5×10^{-3}	2.1×10^{-3}	1.008	1.018	$201 \times 768^{***}$
209	1.5×10^9	34.27	3520.6	-0.29	0.061	6.9×10^{-3}	2.1×10^{-3}	0.994	0.982	$401 \times 1024^{***}$

 $E = 10^{-6}$

210	4×10^8	1.50	232.8	-0.84	0.030	—	—	1.003	1.001	181×512
211	5×10^8	1.79	308.8	-0.78	0.029	—	—	1.000	0.998	181×576
212	6.5×10^8	2.49	471.3	-0.71	0.032	—	—	1.000	1.000	$161 \times 576^{**}$
213	8×10^8	3.41	678.0	-0.65	0.035	5.0×10^{-2}	1.6×10^{-3}	1.001	0.998	181×640
214	1×10^9	4.77	952.5	-0.59	0.039	3.6×10^{-2}	1.5×10^{-3}	0.985	0.986	$193 \times 682^{**}$
215	1.2×10^9	6.19	1208.0	-0.53	0.043	2.9×10^{-2}	1.4×10^{-3}	1.012	1.022	$193 \times 853^{**}$
216	1.5×10^9	8.58	1598.0	-0.48	0.046	2.1×10^{-2}	1.4×10^{-3}	1.010	1.010	201×853
217	2×10^9	12.30	2156.9	-0.43	0.050	1.4×10^{-2}	1.3×10^{-3}	1.003	1.009	$241 \times 853^{**}$
218	2.5×10^9	16.17	2715.3	-0.39	0.053	1.1×10^{-2}	1.2×10^{-3}	1.002	1.009	$321 \times 1024^{**}$
219	3.2×10^9	20.76	3341.7	-0.36	0.054	8.8×10^{-3}	1.2×10^{-3}	1.005	1.016	$321 \times 1024^*$
220	4×10^9	25.65	4075.4	-0.36	0.056	7.4×10^{-3}	1.2×10^{-3}	1.003	1.008	$401 \times 1024^{**}$

$E = 3 \times 10^{-7}$										
221	3.23×10^9	2.42	744.0	-0.72	0.023	—	—	1.006	1.008	241×896
222	4×10^9	3.36	1075.2	-0.67	0.026	5.3×10^{-2}	9.1×10^{-4}	0.996	0.995	$241 \times 896^{***}$
223	5.5×10^9	5.47	1605.4	-0.59	0.034	3.3×10^{-2}	8.3×10^{-4}	1.018	1.010	$241 \times 896^{***}$
224	7×10^9	7.85	2254.7	-0.52	0.038	2.3×10^{-2}	7.5×10^{-4}	1.012	1.019	$301 \times 1024^*$
225	9×10^9	10.96	3047.8	-0.47	0.043	1.6×10^{-2}	7.2×10^{-4}	1.009	1.024	$401 \times 1280^{**}$
226	1.3×10^{10}	17.02	4317.7	-0.42	0.047	1.0×10^{-2}	7.0×10^{-4}	1.000	1.014	$513 \times 1280^{**}$
227	1.8×10^{10}	24.78	5933.6	-0.40	0.050	7.2×10^{-3}	6.9×10^{-4}	1.006	1.028	$641 \times 1365^{***}$

Table A1: Summary table of the quantities of interest for the numerical models computed in this study. These simulations all have $Pr = 1$ and $r_i/r_o = 0.6$. The thermal and viscous boundary layer thicknesses are only given for the cases where boundary layers can be clearly identified. The stars in some selected cases of the last column indicate that those simulations have been computed with an azimuthal symmetry: one star corresponds to a two-fold symmetry, two stars to a four-fold symmetry and three stars to a eight-fold symmetry.

E	Ra_c	m_c
10^{-1}	1.130×10^3	5
3×10^{-2}	1.324×10^3	6
10^{-2}	2.298×10^3	7
3×10^{-3}	5.711×10^3	8
10^{-3}	1.581×10^4	10
3×10^{-4}	5.482×10^4	14
10^{-4}	1.838×10^5	20
3×10^{-5}	7.348×10^5	30
10^{-5}	2.714×10^6	43
3×10^{-6}	1.178×10^7	64
10^{-6}	4.616×10^7	92
3×10^{-7}	2.108×10^8	137
10^{-7}	8.560×10^8	198

TABLE B1. Critical Rayleigh numbers Ra_c and critical azimuthal wavenumbers m_c for the different Ekman numbers employed here. The exact values have been obtained using the open-source eigenmode solver *Singe* (Vidal & Schaeffer 2015), available at <https://bitbucket.org/nschaeff/singe>.

Appendix B. Critical Rayleigh numbers

REFERENCES

- AHLERS, G., GROSSMANN, S. & LOHSE, D. 2009 Heat transfer and large scale dynamics in turbulent Rayleigh-Bénard convection. *Reviews of Modern Physics* **81**, 503–537.
- AMATI, G., KOAL, K., MASSAIOLI, F., SREENIVASAN, K. R. & VERZICCO, R. 2005 Turbulent thermal convection at high Rayleigh numbers for a Boussinesq fluid of constant Prandtl number. *Physics of Fluids* **17** (12), 121701.
- AUBERT, J., BRITO, D., NATAF, H.-C., CARDIN, P. & MASSON, J.-P. 2001 A systematic experimental study of rapidly rotating spherical convection in water and liquid gallium. *Physics of the Earth and Planetary Interiors* **128**, 51–74.
- AUBERT, J., GILLET, N. & CARDIN, P. 2003 Quasigeostrophic models of convection in rotating spherical shells. *Geochemistry, Geophysics, Geosystems* **4**, 1.
- AURNOU, J. M. 2007 Planetary core dynamics and convective heat transfer scaling. *Geophysical and Astrophysical Fluid Dynamics* **101**, 327–345.
- AURNOU, J. M., CALKINS, M. A., CHENG, J. S., JULIEN, K., KING, E. M., NIEVES, D., SODERLUND, K. M. & STELLMACH, S. 2015 Rotating convective turbulence in Earth and planetary cores. *Physics of the Earth and Planetary Interiors* **246**, 52–71.
- BARKER, A. J., DEMPSEY, A. M. & LITHWICK, Y. 2014 Theory and Simulations of Rotating Convection. *ApJ* **791**, 13.
- BERCOVICI, D., SCHUBERT, G., GLATZMAIER, G. A. & ZEBIB, A. 1989 Three-dimensional thermal convection in a spherical shell. *Journal of Fluid Mechanics* **206**, 75–104.
- BLASIUS, H. 1908 Grenzschichten in Flüssigkeiten mit kleiner Reibung. *Z. Math. Phys.* **56**, 1–37.
- BOUBNOV, B. M. & GOLITSYN, G. S. 1990 Temperature and velocity field regimes of convective motions in a rotating plane fluid layer. *Journal of Fluid Mechanics* **219**, 215–239.
- BREUER, M., WESSLING, S., SCHMALZL, J. & HANSEN, U. 2004 Effect of inertia in Rayleigh-Bénard convection. *Phys. Rev. E* **69** (2), 026302.
- BUSSE, F. H. 1970 Thermal instabilities in rapidly rotating systems. *Journal of Fluid Mechanics* **44**, 441–460.
- BUSSE, F. H. & CARRIGAN, C. R. 1974 Convection induced by centrifugal buoyancy. *Journal of Fluid Mechanics* **62**, 579–592.

- BUSSE, F. H. & OR, A. C. 1986 Convection in a rotating cylindrical annulus - Thermal Rossby waves. *Journal of Fluid Mechanics* **166**, 173–187.
- CARDIN, P. & OLSON, P. 1994 Chaotic thermal convection in a rapidly rotating spherical shell: consequences for flow in the outer core. *Physics of the Earth and Planetary Interiors* **82**, 235–259.
- CARDIN, P. & OLSON, P. 2015 8.13 Experiments on Core Dynamics. In *Treatise on Geophysics (Second Edition)*, Second edition edn. (ed. Gerald Schubert), pp. 317–339. Oxford: Elsevier.
- CHANDRASEKHAR, S. 1961 *Hydrodynamic and Hydrodynamic stability*. Oxford University Press.
- CHENG, J. S., STELLMACH, S., RIBEIRO, A., GRANNAN, A., KING, E. M. & AURNOU, J. M. 2015 Laboratory-numerical models of rapidly rotating convection in planetary cores. *Geophysical Journal International* **201**, 1–17.
- CHILLÀ, F. & SCHUMACHER, J. 2012 New perspectives in turbulent Rayleigh-Bénard convection. *The European Physical Journal E* **35** (7).
- CHRISTENSEN, U. R. 2002 Zonal flow driven by strongly supercritical convection in rotating spherical shells. *Journal of Fluid Mechanics* **470**, 115–133.
- CHRISTENSEN, U. R. & AUBERT, J. 2006 Scaling properties of convection-driven dynamos in rotating spherical shells and application to planetary magnetic fields. *Geophysical Journal International* **166**, 97–114.
- CHRISTENSEN, U. R., AUBERT, J., CARDIN, P., DORMY, E., GIBBONS, S., GLATZMAIER, G. A., GROTE, E., HONKURA, Y., JONES, C., KONO, M., MATSUSHIMA, M., SAKURABA, A., TAKAHASHI, F., TILGNER, A., WICHT, J. & ZHANG, K. 2001 A numerical dynamo benchmark. *Physics of the Earth and Planetary Interiors* **128**, 25–34.
- CHRISTENSEN, U. R. & WICHT, J. 2015 8.10 - Numerical Dynamo Simulations. In *Treatise on Geophysics (Second Edition)*, Second edition edn. (ed. Gerald Schubert), pp. 245 – 277. Oxford: Elsevier.
- CORDERO, S. & BUSSE, F. H. 1992 Experiments on convection in rotating hemispherical shells - Transition to a quasi-periodic state. *Geophys. Res. Lett.* **19**, 733–736.
- DAVIDSON, P. A. 2013 Scaling laws for planetary dynamos. *Geophysical Journal International* **195**, 67–74.
- DAVIDSON, P. A. 2015 *Turbulence: an introduction for scientists and engineers*. Oxford University Press.
- DORMY, E., SOWARD, A. M., JONES, C. A., JAULT, D. & CARDIN, P. 2004 The onset of thermal convection in rotating spherical shells. *Journal of Fluid Mechanics* **501**, 43–70.
- ECKE, R. E. & NIEMELA, J. J. 2014 Heat Transport in the Geostrophic Regime of Rotating Rayleigh-Bénard Convection. *Physical Review Letters* **113** (11), 114301.
- EGBERS, C., BEYER, W., BONHAGE, A., HOLLERBACH, R. & BELTRAME, P. 2003 The geoflow-experiment on ISS (part I): Experimental preparation and design of laboratory testing hardware. *Advances in Space Research* **32**, 171–180.
- FUNFSCHILLING, D., BROWN, E., NIKOLAENKO, A. & AHLERS, G. 2005 Heat transport by turbulent Rayleigh Bénard convection in cylindrical samples with aspect ratio one and larger. *Journal of Fluid Mechanics* **536**, 145–154.
- GARCIA, F., SÁNCHEZ, J. & NET, M. 2014 Numerical simulations of thermal convection in rotating spherical shells under laboratory conditions. *Physics of the Earth and Planetary Interiors* **230**, 28–44.
- GASTINE, T. & WICHT, J. 2012 Effects of compressibility on driving zonal flow in gas giants. *Icarus* **219**, 428–442.
- GASTINE, T., WICHT, J. & AURNOU, J. M. 2015 Turbulent Rayleigh-Bénard convection in spherical shells. *Journal of Fluid Mechanics* **778**, 721–764.
- GASTINE, T., WICHT, J., BARIK, A., PUTIGNY, B. & DUARTE, L. D. V. 2016 MagIC v5.4, doi:10.5281/zenodo.51723.
- GILLET, N. & JONES, C. A. 2006 The quasi-geostrophic model for rapidly rotating spherical convection outside the tangent cylinder. *Journal of Fluid Mechanics* **554**, 343–369.
- GILMAN, P. A. 1977 Nonlinear Dynamics of Boussinesq Convection in a Deep Rotating Spherical Shell. I. *GAFD* **8**, 93–135.
- GILMAN, P. A. & GLATZMAIER, G. A. 1981 Compressible convection in a rotating spherical shell - I - Anelastic equations. *ApJS* **45**, 335–349.
- GREENSPAN, H. P. 1968 *The theory of rotating fluids*. Cambridge University Press.

- GROSSMANN, S. & LOHSE, D. 2000 Scaling in thermal convection: a unifying theory. *Journal of Fluid Mechanics* **407**, 27–56.
- GUERVILLY, C. 2010 Dynamos numériques planétaires générées par cisaillement en surface ou chauffage interne. PhD thesis, Sciences de la Terre, univers et environnement, Université de Grenoble, France.
- GUERVILLY, C. & CARDIN, P. 2016 Subcritical convection in a rapidly rotating sphere at low Prandtl number. *ArXiv e-prints*.
- HART, J. E., GLATZMAIER, G. A. & TOOMRE, J. 1986 Space-laboratory and numerical simulations of thermal convection in a rotating hemispherical shell with radial gravity. *Journal of Fluid Mechanics* **173**, 519–544.
- HORN, S. & SHISHKINA, O. 2015 Toroidal and poloidal energy in rotating Rayleigh-Bénard convection. *Journal of Fluid Mechanics* **762**, 232–255.
- INGERSOLL, A. P. & POLLARD, D. 1982 Motion in the interiors and atmospheres of Jupiter and Saturn - Scale analysis, anelastic equations, barotropic stability criterion. *Icarus* **52**, 62–80.
- JARVIS, G. T. 1993 Effects of curvature on two-dimensional models of mantle convection - Cylindrical polar coordinates. *J. Geophys. Res.* **98**, 4477–4485.
- JONES, C. A. 2015 8.05 Thermal and Compositional Convection in the Outer Core. In *Treatise on Geophysics (Second Edition)*, Second edition edn. (ed. Gerald Schubert), pp. 115–159. Oxford: Elsevier.
- JONES, C. A., BORONSKI, P., BRUN, A. S., GLATZMAIER, G. A., GASTINE, T., MIESCH, M. S. & WICHT, J. 2011 Anelastic convection-driven dynamo benchmarks. *Icarus* **216**, 120–135.
- JULIEN, K., AURNOU, J. M., CALKINS, M. A., KNOBLOCH, E., MARTI, P., STELLMACH, S. & VASIL, G. M. 2016 A nonlinear model for rotationally constrained convection with Ekman pumping. *Journal of Fluid Mechanics* **798**, 50–87.
- JULIEN, K., KNOBLOCH, E., RUBIO, A. M. & VASIL, G. M. 2012a Heat Transport in Low-Rossby-Number Rayleigh-Bénard Convection. *Physical Review Letters* **109** (25), 254503.
- JULIEN, K., LEGG, S., MCWILLIAMS, J. & WERNE, J. 1996 Rapidly rotating turbulent Rayleigh-Bénard convection. *Journal of Fluid Mechanics* **322**, 243–273.
- JULIEN, K., RUBIO, A. M., GROOMS, I. & KNOBLOCH, E. 2012b Statistical and physical balances in low Rossby number Rayleigh-Bénard convection. *Geophysical and Astrophysical Fluid Dynamics* **106**, 392–428.
- KING, E. M. & AURNOU, J. M. 2013 Turbulent convection in liquid metal with and without rotation. *Proceedings of the National Academy of Sciences* **110** (17), 6688–6693.
- KING, E. M. & BUFFETT, B. A. 2013 Flow speeds and length scales in geodynamo models: The role of viscosity. *Earth and Planetary Science Letters* **371**, 156–162.
- KING, E. M., SODERLUND, K. M., CHRISTENSEN, U. R., WICHT, J. & AURNOU, J. M. 2010 Convective heat transfer in planetary dynamo models. *Geochemistry, Geophysics, Geosystems* **11**, 6016.
- KING, E. M., STELLMACH, S. & AURNOU, J. M. 2012 Heat transfer by rapidly rotating Rayleigh-Bénard convection. *Journal of Fluid Mechanics* **691**, 568–582.
- KING, E. M., STELLMACH, S. & BUFFETT, B. 2013 Scaling behaviour in Rayleigh-Bénard convection with and without rotation. *Journal of Fluid Mechanics* **717**, 449–471.
- KING, E. M., STELLMACH, S., NOIR, J., HANSEN, U. & AURNOU, J. M. 2009 Boundary layer control of rotating convection systems. *Nature* **457**, 301–304.
- KRAICHNAN, R. H. 1962 Turbulent Thermal Convection at Arbitrary Prandtl Number. *Physics of Fluids* **5**, 1374–1389.
- KUNNEN, R. P. J., GEURTS, B. J. & CLERCX, H. J. H. 2010 Experimental and numerical investigation of turbulent convection in a rotating cylinder. *Journal of Fluid Mechanics* **642**, 445.
- KUNNEN, R. P. J., OSTILLA-MÓNICO, R., VAN DER POEL, E. P., VERZICCO, R. & LOHSE, D. 2016 Transition to geostrophic convection: the role of the boundary conditions. *Journal of Fluid Mechanics* **799**, 413–432.
- LAKKARAJU, R., STEVENS, R. J. A. M., VERZICCO, R., GROSSMANN, S., PROSPERETTI, A., SUN, C. & LOHSE, D. 2012 Spatial distribution of heat flux and fluctuations in turbulent Rayleigh-Bénard convection. *Phys. Rev. E* **86** (5), 056315.

- LIU, Y. & ECKE, R. E. 1997 Heat Transport Scaling in Turbulent Rayleigh-Bénard Convection: Effects of Rotation and Prandtl Number. *Physical Review Letters* **79**, 2257–2260.
- LIU, Y. & ECKE, R. E. 2011 Local temperature measurements in turbulent rotating Rayleigh-Bénard convection. *Phys. Rev. E* **84** (1), 016311.
- ORUBA, L. & DORMY, E. 2014 Predictive scaling laws for spherical rotating dynamos. *Geophysical Journal International* **198**, 828–847.
- PLUMLEY, M., JULIEN, K., MARTI, P. & STELLMACH, S. 2016 The effects of Ekman pumping on quasi-geostrophic Rayleigh-Bénard convection. *Journal of Fluid Mechanics* **803**, 51–71.
- PRANDTL, L. 1905 *Verhandlungen des III. Int. Math. Kongr., Heidelberg, 1904*. Leipzig: Teubner, p. 484–491.
- RHINES, P. B. 1975 Waves and turbulence on a beta-plane. *Journal of Fluid Mechanics* **69**, 417–443.
- ROSSBY, H. T. 1969 A study of Benard convection with and without rotation. *Journal of Fluid Mechanics* **36**, 309–335.
- SCHAEFFER, N. 2013 Efficient spherical harmonic transforms aimed at pseudospectral numerical simulations. *Geochemistry, Geophysics, Geosystems* **14**, 751–758.
- SCHMITZ, S. & TILGNER, A. 2009 Heat transport in rotating convection without Ekman layers. *Phys. Rev. E* **80** (1), 015305.
- SHEW, W. L. & LATHROP, D. P. 2005 Liquid sodium model of geophysical core convection. *Physics of the Earth and Planetary Interiors* **153**, 136–149.
- SHISHKINA, O., STEVENS, R. J. A. M., GROSSMANN, S. & LOHSE, D. 2010 Boundary layer structure in turbulent thermal convection and its consequences for the required numerical resolution. *New Journal of Physics* **12** (7), 075022.
- SODERLUND, K. M., KING, E. M. & AURNOU, J. M. 2012 The influence of magnetic fields in planetary dynamo models. *Earth and Planetary Science Letters* **333**, 9–20.
- STELLMACH, S., LISCHPER, M., JULIEN, K., VASIL, G., CHENG, J. S., RIBEIRO, A., KING, E. M. & AURNOU, J. M. 2014 Approaching the Asymptotic Regime of Rapidly Rotating Convection: Boundary Layers versus Interior Dynamics. *Physical Review Letters* **113** (25), 254501.
- STEVENS, R. J. A. M., CLERCX, H. J. H. & LOHSE, D. 2013 Heat transport and flow structure in rotating Rayleigh-Bénard convection. *European Journal of Mechanics B Fluids* **40**, 41–49.
- STEVENS, R. J. A. M., VERZICCO, R. & LOHSE, D. 2010 Radial boundary layer structure and Nusselt number in Rayleigh-Bénard convection. *Journal of Fluid Mechanics* **643**, 495–507.
- STEVENSON, D. J. 1979 Turbulent thermal convection in the presence of rotation and a magnetic field - A heuristic theory. *Geophysical and Astrophysical Fluid Dynamics* **12**, 139–169.
- SUMITA, I. & OLSON, P. 2003 Experiments on highly supercritical thermal convection in a rapidly rotating hemispherical shell. *Journal of Fluid Mechanics* **492**, 271–287.
- TILGNER, A. & BUSSE, F. H. 1997 Finite-amplitude convection in rotating spherical fluid shells. *Journal of Fluid Mechanics* **332**, 359–376.
- VERZICCO, R. & CAMUSSI, R. 1999 Prandtl number effects in convective turbulence. *Journal of Fluid Mechanics* **383**, 55–73.
- VIDAL, J. & SCHAEFFER, N. 2015 Quasi-geostrophic modes in the Earth’s fluid core with an outer stably stratified layer. *Geophysical Journal International* **202** (3), 2182–2193.
- WICHT, J. 2002 Inner-core conductivity in numerical dynamo simulations. *Physics of the Earth and Planetary Interiors* **132**, 281–302.
- YADAV, R. K., GASTINE, T., CHRISTENSEN, U. R., DUARTE, L. D. V. & REINERS, A. 2016 Effect of shear and magnetic field on the heat-transfer efficiency of convection in rotating spherical shells. *Geophysical Journal International* **204**, 1120–1133.
- ZHONG, J.-Q. & AHLERS, G. 2010 Heat transport and the large-scale circulation in rotating turbulent Rayleigh-Bénard convection. *Journal of Fluid Mechanics* **665**, 300–333.
- ZHONG, J.-Q., STEVENS, R. J. A. M., CLERCX, H. J. H., VERZICCO, R., LOHSE, D. & AHLERS, G. 2009 Prandtl-, Rayleigh-, and Rossby-Number Dependence of Heat Transport in Turbulent Rotating Rayleigh-Bénard Convection. *Physical Review Letters* **102** (4), 044502.